

Extraction of Bend-Resolved Modal Basis in Deformed Multimode Fiber

L. Skvarenina,^{1,2,a)} S. Simpson,³ Y. Alizadeh,¹ and M. Lavery¹

¹⁾*Structured Photonics, James Watt School of Engineering, University of Glasgow, 11 Chapel Lane, Glasgow, G11 6EW, United Kingdom*

²⁾*Department of Physics, Faculty of Electrical Engineering and Communication, Brno University of Technology, Technická 2848/8, Brno, 616 00, Czech Republic*

³⁾*Microphotonics, Institute of Scientific Instruments of the Czech Academy of Sciences, Královopolská 147, Brno, 612 00, Czech Republic*

(Dated: 31 January 2025)

Mode-mixing in fiber from mechanical bending leads to optical perturbations that distort the spatial field profile of coherent beams as they propagate through few or multiple-mode fiber. The observed output from a bent fiber commonly induces complex speckle, which is challenging to directly relate to the bend condition in the fiber, especially for continuously moving systems, such as aerial-deployed fiber or fiber sensors in machinery. We introduce a novel method for constructing a complete mechanically defined modal basis that embodies all fiber deformations resulting from the controlled bending of a multi-mode fiber. This specific basis arises from a differential exchange of power between spatially asymmetric, deformation-dependent orthogonal sets, obtained through singular value decomposition of correlation matrices derived exclusively from speckle patterns at the fiber’s distal end under specific deformation conditions. These spatially quasi-symmetric basis closely resembles a superposition of the fiber’s propagation-invariant modes, with aberrations that result from mechanical deformations. This approach could be readily integrated into mode-division-multiplexing systems to monitor changes in the mechanical variation along deployed fibers for network resilience and fault prediction.

I. INTRODUCTION

In-network fiber sensing tools are a burgeoning research and technology development area that can be used for locating damage detection for deployed infrastructure, robotic sensing, and environmental monitoring, such as earthquake early warning systems for potential seismic hazards, and predictors for network outage^{1–5}. As global capacity demands continue to rise, researchers are advancing multi-mode fiber (MMF) communication technologies that surpass single-mode fibers (SMF) in total capacity and energy efficiency^{6–8}. This progress presents an opportunity to develop new sensing technologies that leverage the unique optical interactions in MMF or even few-mode fibers (FMF) to detect mechanical deformations along the fiber. Unlike SMFs, MMFs experience mode-dependant losses (MDL), temporal group delay (GD) spreading due to modal dispersion and inter-modal coupling that lead to errors in for multiplexed data transmission^{9,10}. Intermodal crosstalk (XT), which inherently transfers energy between adjacent spatial modes during transmission through a shared physical channel, further degrades or completely disrupts transceiver-encoded information. To mitigate these impairments, multiple-input multiple-output (MIMO) digital signal processing (DSP) techniques are employed to accurately track channel impairments and separate parallel data streams. Meanwhile, FMFs supporting a limited number of spatial modes, offer an optimal balance between achieving high data rates over long distances and reducing computational complexity, making MIMO-DSP

even more manageable^{11,12}. Spatial super-channel architecture through MIMO–DSP computationally determines how power has been transferred between modes in a fiber and computes orthogonal modes between the transmitter and receiver that can be used for information encoding^{13–15}. These distortions, which are challenging to decipher, are intrinsically correlated with the physical bending of the fiber. However, accurately characterizing and reconstructing this relationship remains nontrivial without advanced computational techniques^{16–19}.

A widely used approach for analyzing mode propagation through a complex optical channel is singular value decomposition (SVD)^{20,21}. This linear algebraic technique is typically applied to the transfer matrix (TM), which describes the complex amplitude transformation of a predefined set of basis modes as they propagate through the system²². The TM is experimentally measured by injecting known spatial modes into the system and recording their corresponding output fields. These basis modes can be any complete set of spatial modes, such as Laguerre-Gaussian (LG) or Hermite-Gaussian (HG) modes in free-space optics, or Linearly-Polarized (LP) modes in optical fibers with finite modal dimensionality at a given wavelength. Computing the SVD of the transfer matrix (TM) reveals a set of orthogonal input and output modes, forming a basis in which mode coupling is diagonalized. These modes represent linear superpositions of the original basis modes that experience minimal crosstalk and optimal power transmission through the complex optical channel²³. In many cases, the modes obtained from SVD form an optimal, decoupled basis for the system. However, they are not unique and do not inherently provide physical insight into the channel, as they are valid only for a specific instance of inter-channel crosstalk and can change with system per-

^{a)} ✉ Lubomir.Skvarenina@glasgow.ac.uk

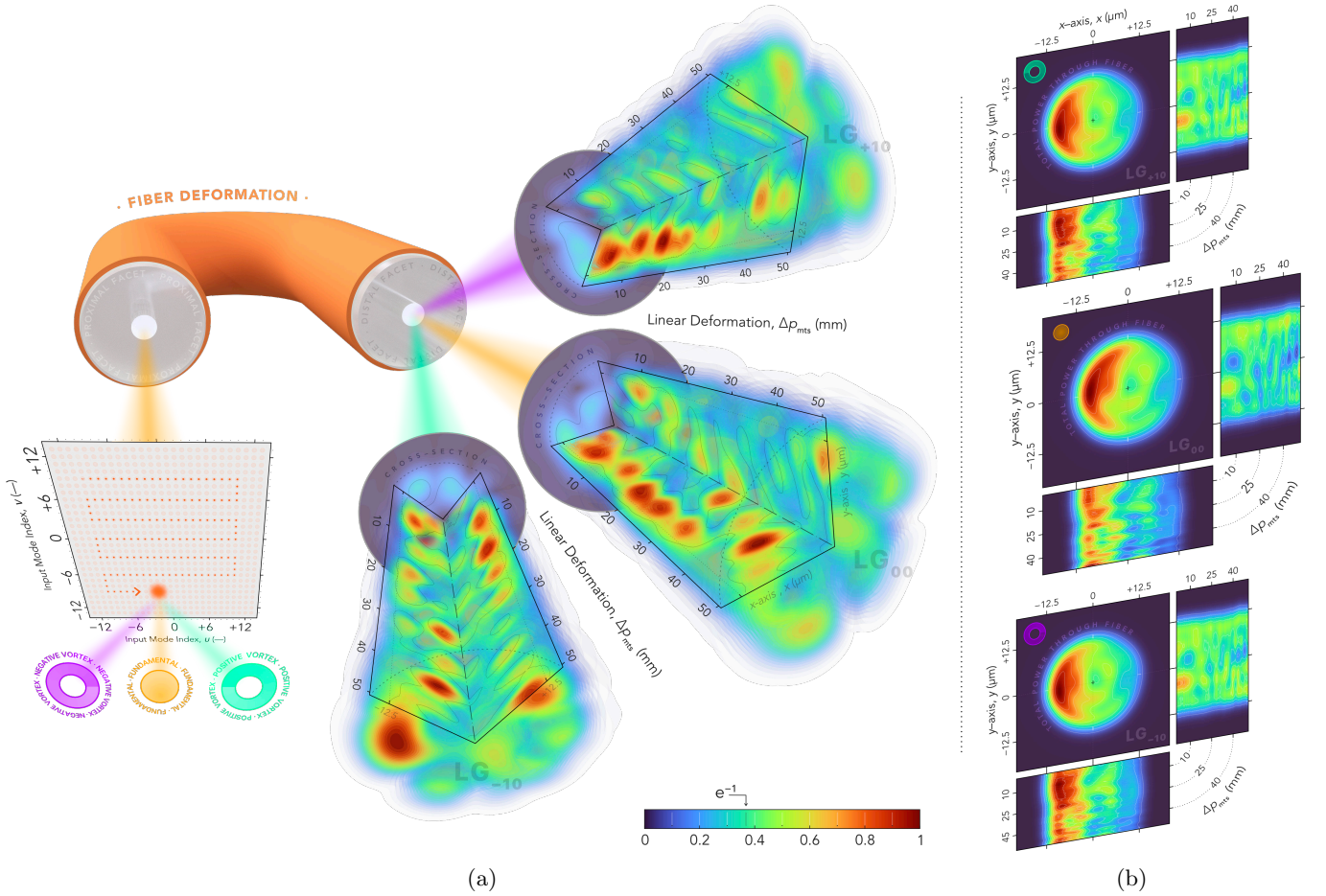


FIG. 1: Illustration of the experimentally acquired field that emerges from a linearly deformed fiber under different coupling conditions $\{LG_{l0}|l \in \{\pm 1, 0\}\}$. (a) Volumetric visualisation of dynamically evolving experimentally obtained speckle patterns amplitude at the distal facet for varying deformations $\Delta p_{mts} = \{0.5 \cdot (p - 1) | p \in \mathbb{N}, p \leq N_B\}$ mm, while keeping the injected beam displacement at the fiber entrance fixed at $(v, u) = (-3, -9)$. Highlighted cross-section of the quarter-volume $|S_\mu^{(p)}(x_0, y_0)|$ for $(x_0, y_0) = \{(-r, 0), (0, r)\}$. (b) Spatial profile of the average cumulative power for all injected beam displacements captures all fiber deformations, $\bar{P}(r, \theta) = (N_B N_S)^{-1} \sum_{p=1}^{N_B} \sum_{\mu=1}^{N_S} |S_\mu^{(p)}(r, \theta)|^2$, with the corresponding cross-section reflecting the impact of each individual deformation on the cumulative output power magnitude, $\bar{P}^{(p)}(x_0, y_0) = N_S^{-1} \sum_{\mu=1}^{N_S} |S_\mu^{(p)}(x_0, y_0)|^2$ for $(x_0, y_0) \in \{(\pm r, 0), (0, \pm r)\}$. Notes: $p \in \{1, \dots, N_B\}$, $N_S = 729$, $N_B = 101$.

turbations²⁴. Accurately predicting intermodal coupling between propagating modes under varying fiber configurations, particularly with continuously changing bending radii along the fiber length, is a highly complex task. While experimentally retrieving the full TM of a fiber is feasible using fast and well-established techniques^{25,26}, aligning these experiments with simulations requires approximating the fiber as a sequence of numerous discrete segments of unequal lengths, each with nearly constant curvature, to account for localized variations in modal coupling^{27,28}. Additionally, since the composition of TMs is generally non-commutative, each approximately uniform segment of a highly nonuniform fiber must be represented by its own TM²⁹. Consequently, mode propagation cannot be accurately described by directly averaging

or summing TMs of segments with similar lengths or curvatures; instead, the correct sequential multiplication of these segment-wise TMs is required to capture the cumulative mode evolution³⁰. Moreover, developing a highly precise model that accounts for micro-local perturbations with high spatial resolution discretization significantly increases computational demands. Micro-bend induced polarization effects, once considered largely independent of the refractive index profile, are now recognized to cause localized birefringence variations, necessitating the inclusion of detailed spatial refractive index variations within TMs. However, this requirement does not pose a challenge for MIMO-DSP-based coherent communication schemes, as the TM is dynamically calculated, and orthogonal transmission channels are continuously opti-

mized to mitigate intermodal and polarization crosstalk. The increasing convergence of hybrid communication and sensing systems, particularly for environmental monitoring and infrastructure security, enables the tracking of variations in SVD modes and their correlation with underlying physical changes along optical fibers^{31,32}.

In this paper, we present a direct framework for constructing a stable, bend-resolved basis of singular modes by analyzing correlation matrices derived from speckle fields of orbital angular momentum (OAM)-carrying light propagating through a multi-mode fiber under systematically controlled bending deformations. Unlike traditional singular modes, which are defined from transfer matrices at fixed bend positions or times and are orthogonal but not unique, our stable bend-resolved singular modes are determined by the physical deformation of the fiber rather than the pseudo-random speckle patterns commonly observed in bent multi-mode optical fibers. As such, these modes can be leveraged to detect mechanical movement, as bend-resolved modes will undergo structural changes in response to different mechanical deformations³³. This feature can serve as an early warning for fiber interference or as a precursor to impending damage to deployed infrastructure. Our approach could be seamlessly integrated into mode-division multiplexing (MDM) coherent communication systems, where the transfer matrix is continuously computed in real-time for a known superposition of spatial fields. By incorporating field trials and machine learning, we anticipate that our novel method could be readily implemented in transceivers to enhance the physical reliability of future MDM fiber communication systems. Additionally, it could be employed for structural health monitoring, detecting resonance variations in large infrastructures such as roads or rail bridges where optical fibers are deployed for communications^{34,35}.

II. METHODOLOGY

In our presented approach, we controllably deform the fiber in a U-shaped configuration using a flat V-groove fiber support, Figs. 1 and 4. The V-groove presses on the fiber changing the radius of curvature of arc resulting in experimentally deterministic planar deformation, as described in Appendix D. These performed experiments can be approximated by simulations using only a small number of segments with predictable lengths and curvatures, according to derived equations in Appendices E and F. To assess the bending effects, the emerged output fields under constant coupling into the fiber were monitored while translating the bend longitudinally in the xz -plane. The set of speckle patterns obtained at each bend position for a constant coupling of a diffraction-limited spot basis was decomposed into bend-related orthogonal bases via SVD. These orthogonal bases were subsequently used to extract a common specifically bend-resolved modal basis corresponding to the applied mechanical deformations.

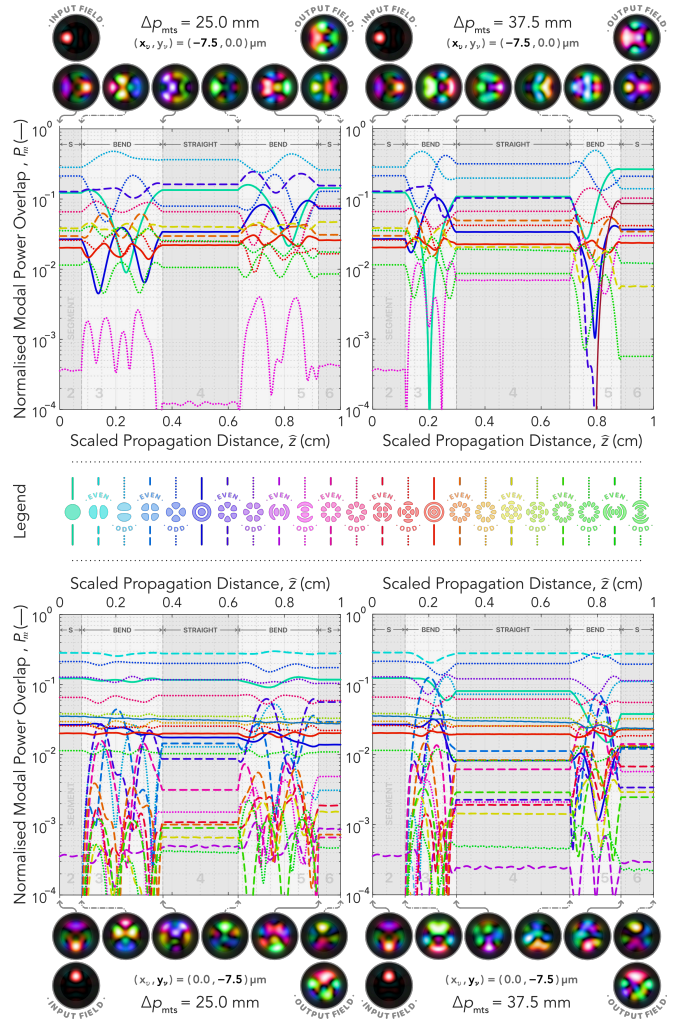


FIG. 2: Intermodal power exchange within the fiber's modal basis is plotted for a propagating optical field through a U-shaped bend subjected to linear deformations of $\Delta p_{\text{mts}} = \{25.0, 37.5\}$ mm, corresponding to bend radii of $r_B = \{79.3, 50.1\}$ mm. The preservation of symmetry in the propagating field is demonstrated through discrete spatial field profiles, derived from an input field defined as a fundamental LG_{00} mode displaced to $\{(x_\nu, y_\nu)\} = \{(-\frac{3}{5}r_{\text{core}}, 0), (0, -\frac{3}{5}r_{\text{core}})\}$ μm and already expressed as a superposition of fiber modes. Note: Segmental lengths $L_{\{2, \dots, 6\}}$ scaled by the factor of $0.01 \cdot (\pi R_0)^{-1}$, reducing the effective propagation distance of the illustrated segments to $\hat{z} = 1$ cm, facilitating the visual interpretability of the intermodal coupling.

A. Propagation Simulations

Simulations of the given fiber geometry were conducted using a modified finite-difference beam propagation method (FD-BPM), as described in³⁶. The simulations revealed that the spatial symmetry of the electric field at the distal end of the fiber $E(r, \phi, z = L_T)$, is highly sensitive to the displacement of the diffraction-

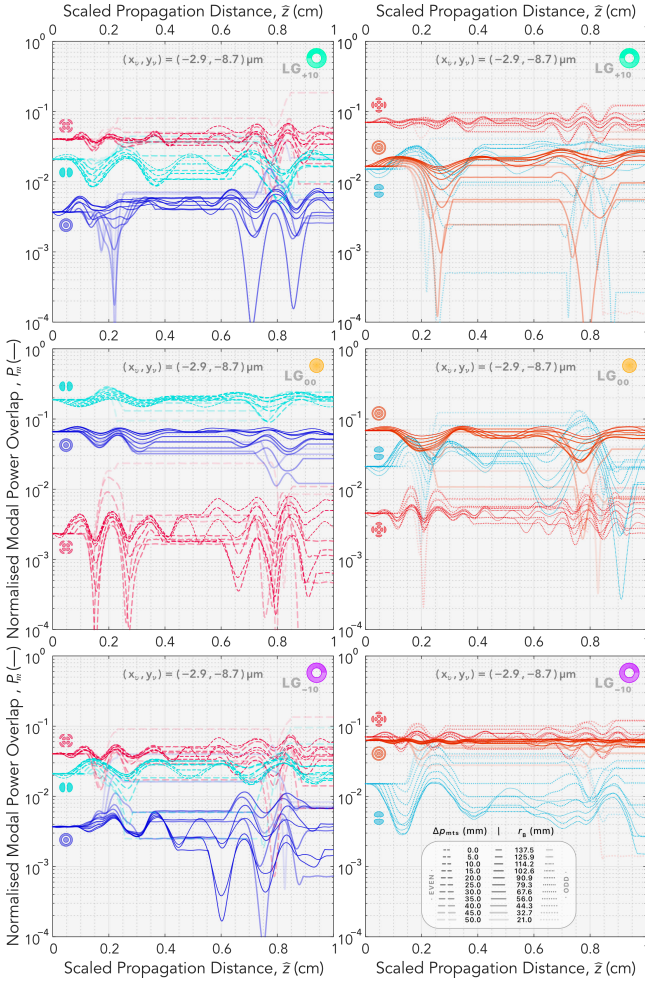


FIG. 3: Variation in power overlap as a function of Δp_{mts} for selected fiber modes $\{LP_{(\ell n)}\}$, where index pairs $(\ell n) \in \{(11), (02), (22), (03)\}$, in a U-shaped bend configuration, involving OAM coupling $\{LG_{\ell 0} | \ell \in \{\pm 1, 0\}\}$, at a fixed fiber entrance position $(x_\nu, y_\nu) = (-\frac{3}{13}r_{\text{core}}, -\frac{9}{13}r_{\text{core}})\mu\text{m}$, where the propagating field is subjected to linear deformations $\Delta p_{\text{mts}} = \{0.0, 5.0, 10.0, \dots, 50.0\}$ mm with a corresponding radii of $r_B = \{137.5, 125.9, 114.2, \dots, 21.0\}$ mm. Note: Segmental lengths $L_{\{2, \dots, 6\}}$ scaled by the factor of $0.01 \cdot (\pi R_0)^{-1}$, reducing the effective propagation distance of the illustrated segments to $\hat{z} = 1$ cm to maintain clarity and enhance the readability of the presented plots.

limited spot on the proximal facet $E(r, \phi, z = 0)$, relative to the axis defined by the transverse bending angle of the curvature with respect to the fiber's longitudinal axis. This is illustrated in Fig. 2 through the normalized modal power overlap of a propagating field with fiber modes for two selected linear deformations, $\Delta p_{\text{mts}} = \{25.0, 37.5\}$ mm, along with the spatial input and output fields, including the corresponding profiles at segments $s = \{2, 3, 4, 5, 6\}$. The propagating field maintains high symmetry when the bending plane aligns with the dis-

placement of the input field relative to the center of the proximal fiber entrance, as demonstrated by the output fields at the top of Fig. 2 for an input field displacement of LG_{00} at $(x_\nu, y_\nu) = (-7.5, 0.0)\mu\text{m}$. Conversely, when the bending plane is perpendicular to the input field displacement at the proximal facet, $(x_\nu, y_\nu) = (0.0, -7.5)\mu\text{m}$, the resulting modal deformation consistently induces pronounced asymmetry in the spatial power distribution, as demonstrated by the bottom axially unbalanced output fields in Fig. 2. A comparison of the modal overlapping powers between the top and bottom plots in Fig. 2 reveals that the nonlinear modal power coupling undergoes a transition to significantly more intricate dynamics, marked by heightened complexity, in the second scenario. Note that the bend radii $r_B = \{79.3, 50.1\}$ mm are strictly given by Eq. (E1), but the lengths $L_s^{(p)} | p = \{51, 76\}$ are reduced by a factor of $0.01 \cdot (\pi R_0)^{-1}$ providing a metric for intermodal power exchange over a shortened propagation distance of $\hat{z} = 1$ cm. Similarly, Fig. 3 illustrates the variation in modal overlap for distinct scenarios involving OAM coupling with $\{LG_{\ell 0} | \ell \in \{\pm 1, 0\}\}$ at a fixed fiber entrance position $(x_\nu, y_\nu) = (-2.9, -8.7)\mu\text{m}$, as shown in Fig. 1. The variation in Fig. 3 is depicted for selected fiber modes, with the left column showing fundamental LP_{02} alongside even modes LP_{11} and LP_{22} , and the right column showing fundamental LP_{03} with odd modes LP_{11} and LP_{22} , subjected to discrete linear deformations with of step of $\delta p_{\text{mts}} = 5$ mm in range of $\Delta p_{\text{mts}} = (0-50)$ mm given by MTS, corresponding to bend radii in range $r_B = (137.5-21.0)$ mm with step of $\delta r_B = 11.6$ mm. Emerged beam over an extended distance through a fiber curvature oriented within an arbitrary plane demonstrates that the phase delays, altered by modal conformations, inherently concentrate energy exchange within the plane of the bend. It is important to note, however, that these findings are derived from a model where the bend is idealized as a curvature confined to a single longitudinal plane, with a spatially uniform deformation of the transverse refractive index profile, devoid of perturbations from micro-bends, and characterized by a twist rate that asymptotically diminishes to zero over an infinite propagation length.

B. Experimental Measurements

The complex wavefront of the output speckled from the fiber was measured for a series of spatial positions over the proximal facet using diffraction-limited foci. This positions were equally spaced in a square Cartesian grid defined as $\{(x_\nu, y_\nu)\} = \{f_L \lambda (d_{\nu\nu})^{-1}, f_L \lambda (d'_{\nu\nu})^{-1}\}$, where f_L incorporates focal lengths of each lens in front of the fiber, the granting spacing is determined by the resolution and pixel pitch of the SLM ($d = n_{[\text{px}]} p_{[\mu\text{m}]}$) and index pairs $(\nu, \nu) \in \mathbb{Z}$. In addition to sweep with a Gaussian spot (LG_{00}) to achieve different mode excitations that allows testing bending sensitivity under different launch conditions, experiments were also conducted by

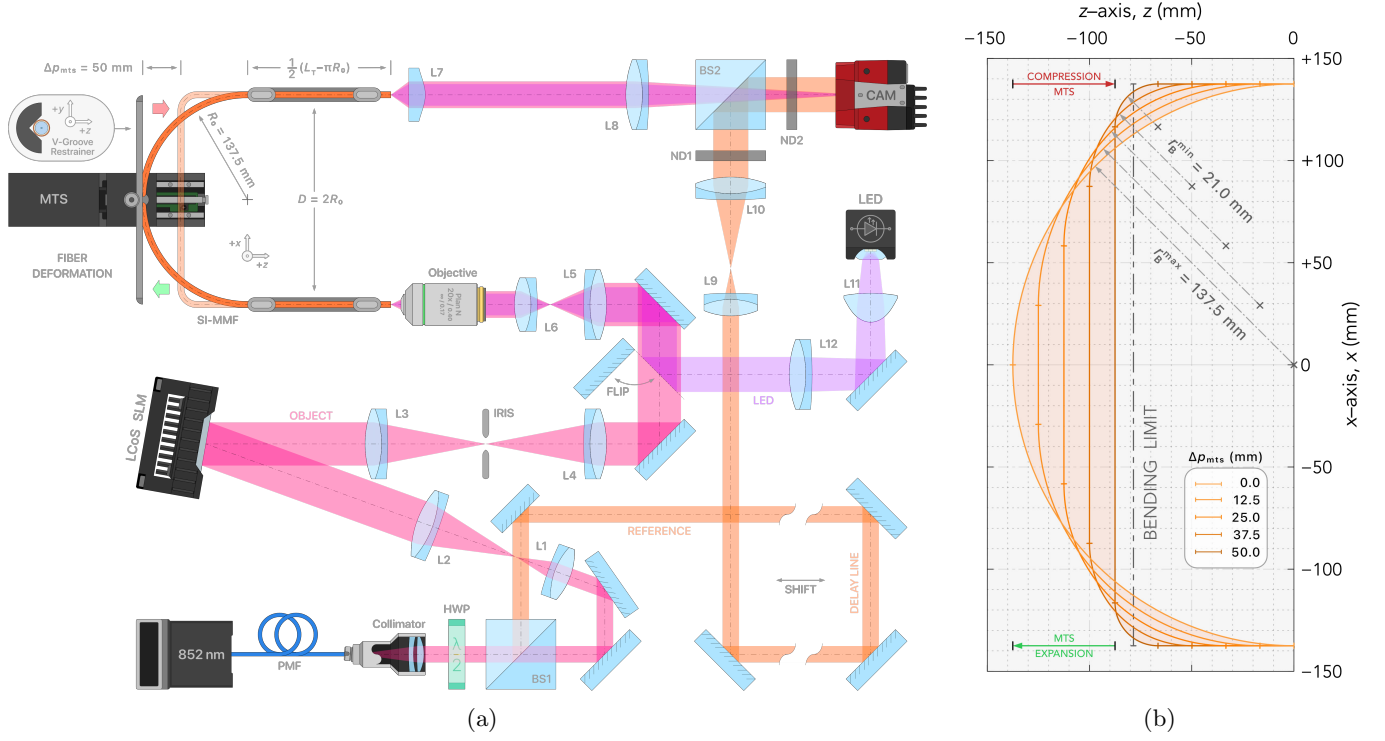


FIG. 4: A system for measuring the distorted fields arising from a controllably deformed fiber. (a) Experimental optical arrangement for scanning through the SI-MMF across multiple bending positions. (b) Model of the idealized geometric representation of a U-shaped fiber configuration under predictable deformations. Fiber parameters: SiO₂ core with $\varnothing_{\text{core}} = (25 \pm 3) \mu\text{m}$, F:SiO₂ cladding with $\varnothing_{\text{cladd}} = (125 \pm 2) \mu\text{m}$, NA = 0.100 ± 0.015 , $\alpha \approx 0.048 \text{ dB m}^{-1}$ at $\lambda = 850 \text{ nm}$; Linear MTS set in discrete positions $\Delta p_{\text{mts}} = \{0.0, 0.5, \dots, 50.0\}$ mm with an accuracy of $\bar{\delta}_{\text{mts}} = \pm 1.6 \mu\text{m}$. Notes: BS – beamsplitter, CAM – camera, HWP – half-wave plate, SI-MMF – step-index multimode fiber, L – lens, LCoSSLM – liquid crystal on silicon spatial light modulator, MTS – motorised translation stage, ND – neutral-density filter, PMF – polarisation maintaining fiber.

incorporating orbital angular momentum (OAM) with $\text{LG}_{\pm 10}$. The following notation is independent of specific beam injection conditions into the fiber, as the resulting fields from the injected spot-basis were processed independently for displacements with a constantly injected LG beam. In this manner in each deformation position $\Delta p_{\text{mts}} = \{0.0, 0.5, \dots, 50.0\}$ mm imposed by the linear MTS, light was injected into the proximal facet for input modes with indices $\nu, \nu \in [-13, +13]$, as illustrated in Fig. 1a. Axial coupling at the core centre $(\nu, \nu) = (0, 0)$ predominantly excites fundamental modes, whereas increasing eccentric displacement of the injection spot facilitates power coupling primarily into higher-order modes, albeit with higher loss. As the displacement of the input beam excites a subset of modes with varying power distributions, the bending characteristics determined by the intermodal coupling are necessarily influenced by this position. This spatial dependency must be incorporated to accurately describe the dynamic behavior of the modes under different bending deformations, ensuring precise comprehension of modal interactions and power exchange within the fiber. The resultant electric fields, forming speckle patterns at the

distal facet for various coupling displacements and deformations induced by the MTS can be expressed as $S_{\mu}^{(p)}(r, \theta) = E_{\mu}^{(p)}(r, \theta, z | z = L_T)$, where global index $\mu = \mu(\nu, \nu)$ maps each pair ν, ν to a particular integer $\mu \in \mathbb{N}$. Considering the aforementioned scanning over proximal facet, the total number of speckle patterns $N_S = 729$ was recorded for number of bends $N_B = 101$. The density of the coupling grid is highly overestimated, considering the fiber can theoretically support only $N_M \approx 23$ modes. Nevertheless, scanning over this high-density grid generates a large set of speckle patterns that not only sufficiently excite the fiber's modal space but also enable the tracking of dynamic changes in an almost continuous manner across displacements on the fiber facet.

C. Singular Value Decomposition

As the examination of propagation dynamics through various lateral displacements at the fiber entrance allows for a comprehensive and continuous monitoring of power exchange, the total information captured within the

speckle space (corresponding to the input spot-like basis) becomes overestimated and redundant, since $N_M \ll N_S$. Although a sufficiently large set of speckle patterns can represent any arbitrary field within the fiber as a linear combination of these patterns, the speckle basis is overcomplete and lacks orthogonality, i.e. $\langle S_\mu | S_\eta \rangle \neq 0$ for $\mu \neq \eta$. Tracking deformation dynamics is significantly more efficient when utilizing a basis that matches the fiber's modal space span to sufficiently cover all modal interactions under deformation. To achieve this, we employ dimensionality reduction via SVD, which captures power exchange through the most significant modes, optimizing the efficiency of deformation dynamics analysis within the fiber's modal space³⁷. Each set of speckle patterns that emerged through constant fiber deformation from multiple lateral displacements at proximal facet $\{S_1^{(p)}, S_2^{(p)}, \dots, S_{N_S}^{(p)}\}$ is projected onto itself to construct bend-dependent correlation matrices $\mathbf{M}^{(p)} \in \mathbb{C}^{N_S \times N_S}$ as follows

$$M_{\mu\eta}^{(p)} = \int_{-\pi}^{+\pi} \int_0^\infty \{S_\mu^{(p)}(r, \theta)\}^* \cdot S_\eta^{(p)}(r, \theta) r dr d\theta, \quad (1)$$

where each $[\langle S_\mu^{(p)} | S_\eta^{(p)} \rangle] = \mathbf{M}^{(p)}$ produce a square hermitian matrix $M_{\mu\eta}^{(p)} = \{M_{\eta\mu}^{(p)}\}^*$. To elucidate the intrinsic modal dynamics and interactions within the fiber, these matrices are subjected to SVD, facilitating the extraction of linearly independent orthogonal components that convey the dominant optical power distribution while spanning the fiber's modal space³⁸. As a result, each matrix arising from fiber deformation, represented in its factorized form as

$$\mathbf{M}^{(p)} = \mathbf{U}^{(p)} \mathbf{\Sigma}^{(p)} \{\mathbf{V}^{(p)}\}^H = \sum_{\tilde{k}=1}^{N_S} \sigma_{\tilde{k}}^{(p)} \mathbf{u}_{\tilde{k}}^{(p)} \{\mathbf{v}_{\tilde{k}}^{(p)}\}^H, \quad (2)$$

is uniquely determined due to its Hermitian property, which satisfies $\mathbf{M} = \mathbf{M}^H = (\mathbf{U}\mathbf{\Sigma}\mathbf{V}^H)^H = \mathbf{V}\mathbf{\Sigma}\mathbf{U}^H$, implying $\mathbf{V} = \mathbf{U}$. Thus the each SVD can be interpreted as an eigendecomposition of overdetermined Hermitian matrix expressed as $\mathbf{M} = \mathbf{V}\mathbf{\Lambda}\mathbf{V}^H$, where singular values ($\sigma_{\tilde{k}}$) are equivalent to the square roots of the eigenvalues ($\lambda_{\tilde{k}}$), since $\mathbf{\Lambda} = \mathbf{\Sigma}^2$. Consequently, the diagonal elements of $\mathbf{\Sigma}^2 = \mathbf{V}^H\mathbf{M}\mathbf{V}$ represent the eigenvalues of \mathbf{M} , while the columns of \mathbf{V} serve as the corresponding eigenvectors. As the singular values in each overdetermined non-unitary matrix (of rank $\tau = N_S$) are arranged in descending order as $|\sigma_{\tilde{k}}|^2 \geq |\sigma_{\tilde{k}+1}|^2 \geq 0 \forall \tilde{k} \in \{1, 2, \dots, N_S\}$, it should be possible to identify a cut off value ($\epsilon > 0$) in coupling strengths, that determine the true rank (τ_X) of the matrix \mathbf{M} equivalent to fiber modal space as $\text{rk}(\mathbf{M}) \equiv N_M$, such that $|\sigma_{\tilde{k}}|^2 \leq \epsilon \forall \tilde{k} > \tau_X$ and $|\sigma_{\tilde{k}}|^2 \gg \epsilon \forall \tilde{k} \leq \tau_X$. In an ideal scenario, unequivocally devoid of noise or other errors, the true rank of the system precisely matches the number of fiber modes, $\tau_X = N_M$. Conversely, the presence of noise or experimental imperfections can artificially inflate the rank, resulting in $\tau_{\tilde{X}} > N_M$, thereby obscuring the true modal bandwidth of the fiber.

III. RESULTS

According to matrix factorization and rank determination as described in Section II C, it is possible to construct a complete orthonormal finite basis of effective modes for the fiber as

$$\Psi_\eta^{(p)}(r, \theta) = \sum_{\mu=1}^{N_S} \{\sigma_\eta^{(p)}\}^{-\frac{1}{2}} V_{\mu\eta}^{(p)} S_\mu^{(p)}(r, \theta), \quad (3)$$

which produces a set of linearly independent modes. These singular modes represent weighted linear combinations of the fiber's intrinsic modes, forming a compact, low-rank approximative basis that spans the fiber's modal space and is capable of representing any arbitrary optical field emerging from the same fiber. For a specific bend configuration, the singular modes within each set are inherently orthogonal, rigorously defined as $\langle \Psi_\eta^{(p)} | \Psi_{\eta'}^{(p')} \rangle = \delta_{\eta\eta'} \Leftrightarrow p = p'$, thereby eliminating crosstalk between modes. The orthogonality fundamentally arises from the singular value decomposition, where the singular value matrix, expressed as $\mathbf{V}^H\mathbf{M}\mathbf{U} = \mathbf{\Sigma}$, is strictly diagonal and real, thereby ensuring the modes' linear independence and complete decoupling³⁹. The singular values can be interpreted as the transmission coefficients for each modal component, reflecting their specific losses throughout the system. Omitting their square root inverse in Eq. (3) produces the same orthogonal set while preserving the power ratio of the injected light redistributed among the fiber modes, meaning the resulting set would no longer be orthonormal. Consequently, each set constitutes an optimal and comprehensive propagation non-invariant basis for accurately reconstructing any arbitrary optical field within the same fiber.

As the singular modes within each set are linear combinations of the fiber's inherent, mutually orthogonal eigenmodes, any optical field emerging from the fiber can be effectively approximated by projecting it onto these singular mode sets, regardless of the specific deformations from which the modes were originally derived. However, this approximation becomes limited when tighter bends cause the critical angle for total internal reflection to be exceeded. In such cases, the modes of highest order may be effectively lost to the cladding, as they no longer satisfy the conditions necessary for confinement within the fiber core. In other words, the set of singular modes derived from speckle patterns at shallower bend angles preserves the fiber's modal bandwidth, enabling the expansion of any arbitrary field despite the presence of deformations. Conversely, the set of singular modes constructed from speckle patterns at tighter bends progressively excludes highest-order modes, thereby limiting the modal bandwidth. As a result, only speckle patterns acquired at equal or tighter bend radii can be fully expanded within this basis. The dynamic progression of the selected sets of singular modes, along with their corresponding relative power distribution under various linear deformations, is illustrated in Fig. 5a. As depicted

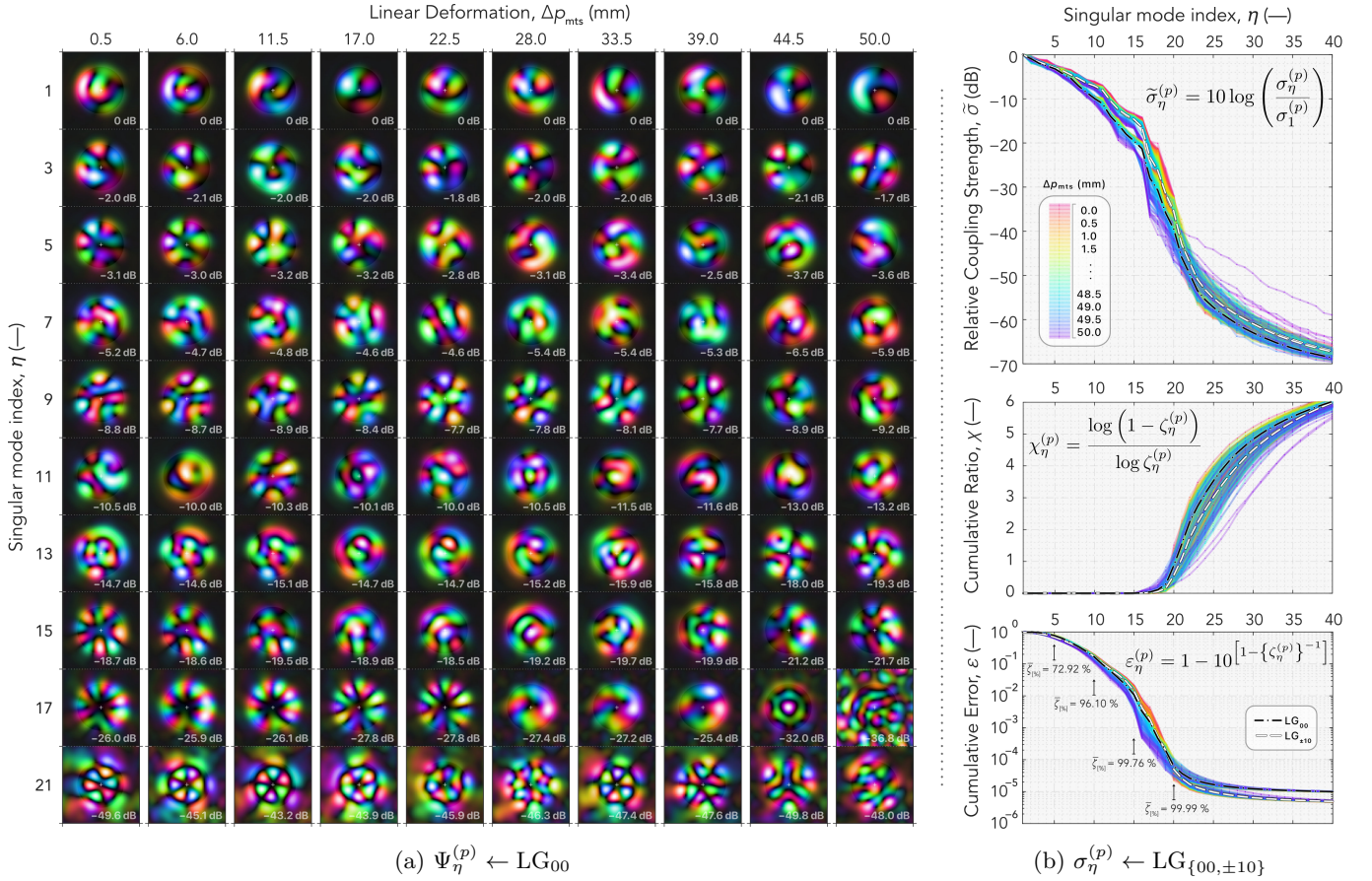


FIG. 5: An overview of the constructed deformation-related sets of singular modes, ordered by decreasing singular values. (a) A representative plot shows the variation in the singular modes spatial profile, where $\langle \Psi_{\eta}^{(p)} | \Psi_{\eta'}^{(p')} \rangle = \delta_{\eta\eta'} \Leftrightarrow p = p'$, under quasi-equivalent coupling strength as the fiber undergoes linear deformation via MTS translation, based on speckle patterns generated by LG_{00} mode coupling. (b) Relative coupling strengths with respect to zero for all linear deformations Δp_{mts} , with different plots of singular values derived from the cumulative sum $\zeta_{\eta}^{(p)} \in [0, 1]$, expressed as $\zeta_{\eta}^{(p)} = \sum_{i=1}^{\eta} \sigma_i^{(p)} (\sum_{i=1}^{N_S} \sigma_i^{(p)})^{-1}$. Notes: The average of the given σ quantities is indicated by the black dash-dotted line for LG_{00} and the white dashed line for $\text{LG}_{\pm 10}$, respectively.

in the plot of relative coupling strength ($\tilde{\sigma}_{\eta}^{(p)}$) dependent on the singular mode index (η) for all linear deformations in Fig. 5b, where the black dot-dashed and white dashed lines, representing the mean values of light injection with LG_{00} and $\text{LG}_{\pm 10}$, demonstrate that coupling with orbital angular momentum (OAM) significantly enhances the excitation of higher-order modes within the fiber's modal space. Notably, the nearly identical overlap of the dashed mean values for $\text{LG}_{\pm 10}$ further emphasizes this effect. Furthermore, a distinct and continuous decay in relative coupling strength is observed as the fiber deformation evolves. This progression is visually illustrated by a color gradient, transitioning from $\tilde{\sigma}_{\eta}^{(1)}$ (red) at $\Delta p_{\text{mts}} = 0$ mm to $\tilde{\sigma}_{\eta}^{(N_B)}$ (purple) at $\Delta p_{\text{mts}} = 50$ mm, highlighting the impact of altered deformations. Besides the traditional plot of coupling strengths, Fig. 5b also depicts plots of quantities such as the ratio ($\zeta_{\eta}^{(p)}$) and error ($\varepsilon_{\eta}^{(p)}$), which were derived from the cumulative sum ex-

pressed as $\zeta_{\eta}^{(p)} = \sum_{i=1}^{\eta} \sigma_i^{(p)} (\sum_{i=1}^{N_S} \sigma_i^{(p)})^{-1}$, enhancing the transition in the cumulative power addition of modes. It is clear that the light power is coupled into the highest-order modes to a minimal extent, as the fiber theoretically supports 23 modes at the given wavelength, with $\tilde{\sigma}_{N_M}^{(p)}$ varying in the level range of (50–55) dB, while the cumulative power of singular modes at $\eta = 18$ has already achieved $\bar{\zeta}_{18}^{(p)} = 99.99\%$. This can be attributed to the use of a spot-like basis for mode excitation, which, while advantageous for imaging purposes through the fiber^{40–42}, fails to optimize the capacity for spatial channels from an information theory perspective as it is not a truly orthogonal basis set in the strict sense. Nevertheless, it was chosen because the correlative analysis of the fiber's response to linear deformation can be mapped to specific points on an equidistant Cartesian grid across the fiber facet, which is more intuitive to interpret in the nearest orthogonal basis, as demonstrated in Fig. 10.

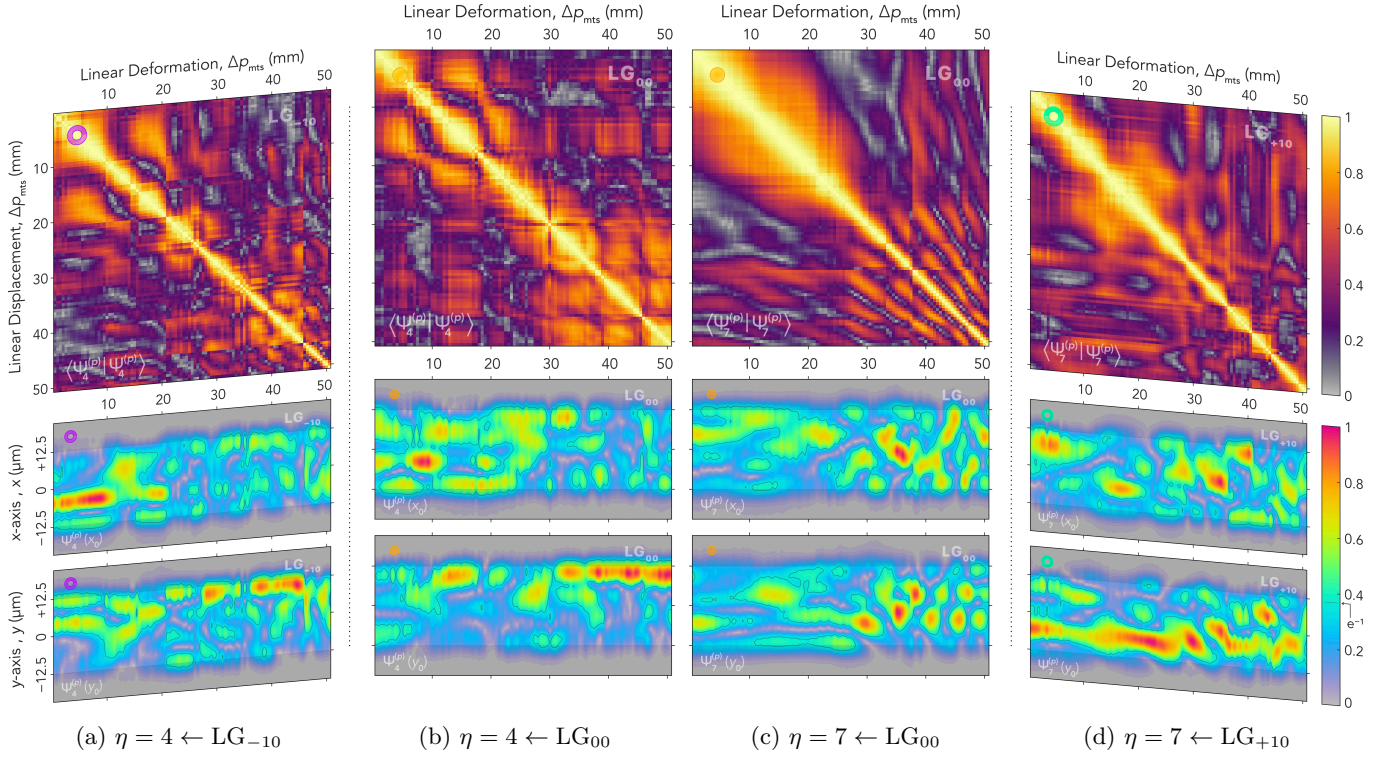


FIG. 6: Examination of the correlation between singular modes with quasi-equivalent coupling strength for all linear deformations, where $\langle \Psi_{\eta}^{(p)} | \Psi_{\eta}^{(p')} \rangle \neq 0 \Leftrightarrow p \neq p'$. As the singular modes differ spatially under coupling with an ordinary LG_{00} beam compared to $LG_{\pm 10}$, the correlation matrices has to differ as well; compare (a, b) $\eta = 4$ and (c, d) $\eta = 7$. A corresponding cross-section through their spatial shape is given by $|\Psi_{\eta}^{(p)}(x_0, y_0)|$ for $(x_0, y_0) = \{(\pm r, 0), (0, \pm r)\}$, where the field cross-sections for each Δp_{mts} in (b, c) are orthogonal to each other. Note: $\Delta p_{mts} = \{0.0, 0.5, \dots, 50.0\}$ mm.

As anticipated, the singular modes within a given set corresponding to a specific deformation exhibit perfect orthogonality, $\langle \Psi_{\eta}^{(p)} | \Psi_{\eta}^{(p')} \rangle = \delta_{\eta p p'} \Leftrightarrow p = p'$. However, this orthogonality does not naturally extend across sets associated with different linear deformations, $\langle \Psi_{\eta}^{(p)} | \Psi_{\eta}^{(p')} \rangle \neq 0 \Leftrightarrow p \neq p'$, where the inner product between modes constructed from different deformations is non-zero. The correlation matrices, along with the cross-sectional views of the spatial shapes of singular modes for $\eta = \{4, 7\}$ across varying linear displacements, are shown in Fig. 6. The resulting correlation matrices display dynamic behavior akin to that of the originally constructed matrices derived from the speckle patterns, as illustrated in Fig. 10. In this framework, all acquired dynamic variations are fully captured within bases that are isomorphic to the dimensionality of the fiber's modal space. Note that the axial cross-sections through emerged fields at $(x_0, y_0) = \{(\pm r, 0), (0, \pm r)\}$ shown in Figs. 6b and 6c are mutually orthogonal. The matrices and corresponding fields exhibit differences when coupled with LG_{00} and $LG_{\pm 10}$ modes, while coupling with modes of opposite angular momentum (such as $l = -1$ and $l = +1$ with the equal η) yields nearly identical results, making the cross-sections in Figs. 6a and 6d nearly orthogonal.

As the aforementioned effort to reduce the dimensionality of the speckle basis to a complete orthogonal sets that spans the fiber's modal space, we propose utilizing SVD once again to derive a robust common basis that effectively captures all dynamic interactions induced in the fiber over the given span of deformations. To accomplish this, we concatenate all singular mode sets corresponding to various bend deformations into a unified over-complete set $\Psi_{\rho}(r, \theta)$, with the original integers η, p mapped to a single index $\zeta = \zeta(\eta, p) \in \mathbb{N}$ which lacks orthogonality between the singular modes with unequal p indices. Accordingly to Eq. (1) is possible to construct a unified correlation super-matrix as $\langle \Psi_{\zeta} | \Psi_{\zeta'} \rangle = \mathbf{K}$, where $\mathbf{K} \in \mathbb{C}^{(\tau \times N_B) \times (\tau \times N_B)}$. Following this, by applying factorization outlined in Eq. (2) and subsequent construction detailed in Eq. (3), enables the formation of a robust modal set as

$$\widehat{\Psi}_{\rho}(r, \theta) = \sum_{\zeta=1}^{\tau \times N_B} \sigma_{\zeta}^{-\frac{1}{2}} V_{\zeta \rho} \Psi_{\zeta}(r, \theta), \quad (4)$$

which represents a common or global set of modes that efficiently spans the entire fiber's modal space, while capturing the deformation-induced variations un-

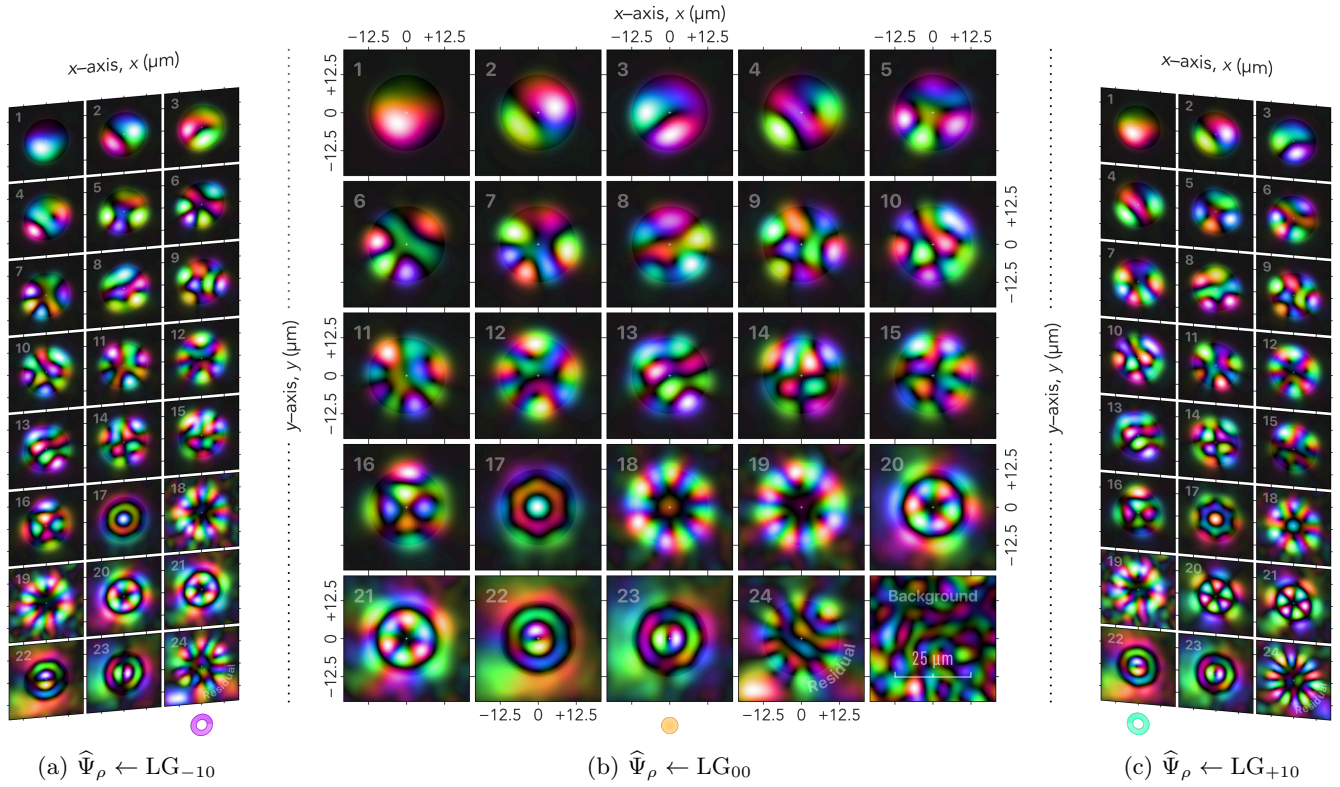


FIG. 7: The common modal basis, obtained through a second SVD of the concatenated mode sets corresponding to individual bends, encapsulates the global bend-resolved modal structure, encompassing all fiber conformations within the range of deformations imposed by the MTS, while exhibiting superior spatially power-balanced uniformity compared to the initial modal basis derived from the first SVD. It encapsulates the most stable and deformation-recurrent characteristics of the fiber’s modal space, emphasizing resilient modal patterns that endure across diverse fiber configurations and coupling conditions. (a, b, c) Notably, this common basis retains coherent spatial profiles for coupling with $\text{LG}_{\ell 0}$ modes, where $\ell = \pm 1, 0$, even though distinct coupling scenarios involving LG modes engender diverse spatial distributions of singular modes associated with fiber deformation as characterized by the first SVD.

der the specific bend scenarios considered. This common basis set, illustrated in Fig. 7, exhibits a higher degree of symmetry compared to the singular bases shown in Fig. 5a. Notably, the highest-order singular modes $\hat{\Psi}_\rho|_{\rho=\{20,\dots,23\}}$, closely resemble the fiber’s doubly degenerate, propagation-invariant $\text{LP}_{ln}|_{ln=\{\pm 32,\pm 13\}}$ under the weakly guiding approximation, as illustrated in Fig. 11a. In contrast, other singular modes, such as $\hat{\Psi}_\rho|_{\rho=\{17,18,19\}}$, resemble axially power-balanced linear combinations of the fiber’s $\text{LP}_{ln}|_{ln=\{03,\pm 51\}}$ modes, characterized by nearly indistinguishable propagation constants, as illustrated in the middle plot of Fig. 11b.

We observed that the spatial configuration of this basis remains consistent, regardless of the subsample of speckle patterns selected from the input basis, as long as the condition $N_S \geq N_M$ is rigorously satisfied. Moreover, selecting a subset of speckles from the off-center, laterally shifted spot basis results in different spatial fields for the singular modes, while the spatial configuration of the common basis remains unchanged, apart from a global phase shift. Additionally, this

basis set remains invariant even when the number of bends involved in the factorization is subsampled within the given span of deformations, as demonstrated in Fig. 8. In this context, the spatial configuration remains invariant, provided that the deformation space spans a dimensionality sufficient to fully encompass the modal space of the fiber. Theoretically it is crucial to incorporate a sufficient number of deformations, at least commensurate with the fiber’s modal bandwidth; otherwise, the dominant intermodal coupling effects induced by deformation cannot be fully captured across the fiber’s entire modal space. Nevertheless, as illustrated in Fig. 8b, subsampling the given span of deformations according to $\Delta \tilde{p}_{\text{mts}} = \{\delta p_{\text{mts}}^{(i)} \cdot (p-1) \mid p \in \mathbb{N}, p \leq \tilde{N}_B^{(i)}\}$ mm, where $\{(\delta p_{\text{mts}}^{(i)}, \tilde{N}_B^{(i)}) \mid i=1,2,3,4\} = \{(51, 1.0 \text{ mm}), (26, 2.0 \text{ mm}), (17, 3.0 \text{ mm}), (13, 4.0 \text{ mm})\}$ and calculating the overlap integral $\langle \hat{\Psi}_\rho | \tilde{\Psi}_{\rho'}^{(i)} \rangle$ between the fully spanned basis (shown in Fig. 7) and its subsampled counterparts (depicted in Fig. 8a), demonstrates that the spatial consistency of the bases is preserved. Incorporating fidelity metrics, defined

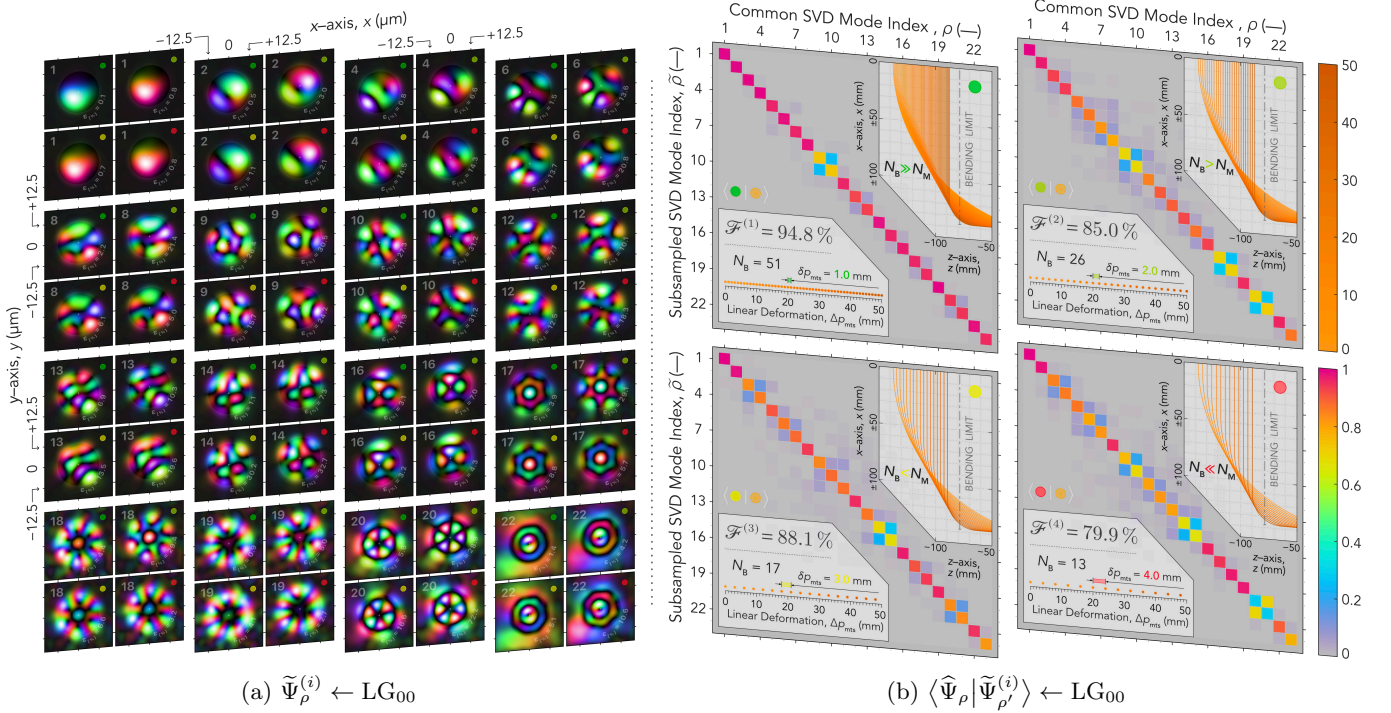


FIG. 8: An evaluation of modal stability is conducted for the common basis constructed from subsampled linear deformations, compared to the basis derived from the complete set of experimentally acquired deformations. (a) An analysis of individual subsample modal shape variations is presented in relation to the corresponding mode-specific error ($\varepsilon_{[\%]}$), which can be interpreted as per-modal infidelity. (b) Overlap stability matrices quantify the consistency between the originally constructed common SVD basis and its subsampled versions, with a progressively increasing step size (δp_{mts}) that reduces the number of included deformation sets (\tilde{N}_B). The degree of this consistency is rigorously evaluated through fidelity metrics, defined as $\mathcal{F}^{(i)} = \text{tr}\{N_M^{-1} |\langle \hat{\Psi}_\rho | \tilde{\Psi}_{\rho'}^{(i)} \rangle|^2\} \%$. Note: $\Delta \tilde{p}_{\text{mts}} = \{\delta p_{\text{mts}}^{(i)} \cdot (p-1) \mid p \in \mathbb{N}, p \leq \tilde{N}_B^{(i)}\}$ mm, where $\{(\delta p_{\text{mts}}^{(i)}, \tilde{N}_B^{(i)}) \mid i=1,2,3,4\} = \{(51, 1.0 \text{ mm}), (26, 2.0 \text{ mm}), (17, 3.0 \text{ mm}), (13, 4.0 \text{ mm})\}$.

as $\mathcal{F}^{(i)} = \text{tr}\{N_M^{-1} |\langle \hat{\Psi}_\rho | \tilde{\Psi}_{\rho'}^{(i)} \rangle|^2\} \%$, facilitates a precise and rigorous quantitative assessment of mode alignment across variations induced by sparse subsampling. For scenarios where $\tilde{N}_B \geq N_M$, the fidelity achieves $\mathcal{F}^{(1)} = 94.8 \%$ and $\mathcal{F}^{(2)} = 85.0 \%$ for step sizes $\delta p_{\text{mts}}^{(1)} = 1.0 \text{ mm}$ and $\delta p_{\text{mts}}^{(2)} = 2.0 \text{ mm}$, respectively. Notably, the sparse overlap matrix preserves a predominantly diagonal structure, even for subsampled deformation sets that do not fully span the fiber's modal space, with a step size of $\delta p_{\text{mts}}^{(1)} = 3.0 \text{ mm}$ achieving a fidelity of $\mathcal{F}^{(3)} = 88.1 \%$, and $\delta p_{\text{mts}}^{(1)} = 4.0 \text{ mm}$ achieving $\mathcal{F}^{(4)} = 79.9 \%$. It is noteworthy that the fidelity for $\tilde{N}_B^{(3)} = 17$ surpasses that for $\tilde{N}_B^{(2)} = 26$. However, in second case where $\tilde{N}_B > N_M$, the power coupling appears to be confined exclusively to neighboring mode pairs (degenerate pair), as depicted in Fig. 8b. This phenomenon is likely driven exclusively by linear combinations of modes sharing equivalent modal group delays, defined by their nearly identical propagation constants (see attachment Fig. 11). For instance, examine and compare the singular modes $\tilde{\Psi}_{\{9,10\}}^{(i)} \mid i=\{1,2\}$, as depicted in Fig. 8a, or overlap integral matrices for singular

modes $\tilde{\Psi}_{\{21,22\}}^{(i)} \mid i=\{2,4\}$, which resemble a $\text{LP}_{\pm 32}$ mode. It is important to emphasize that deriving this universal bend-resolved set cannot be achieved through a direct application of SVD on a correlation matrix constructed from the ensemble of speckle patterns encompassing all input field displacements and bending configurations.

As depicted in the cross-section of the average cumulative power in Fig. 1b and the orthogonal cross-section of singular modes with quasi-equivalent coupling strengths in Figs. 6b and 6c, the complexity of modal interactions steadily intensifies as increasing linear deformations directly lead to higher curvature in the bend segments. To better elucidate the contributions of specific deformation ranges, a reduced common basis was derived by isolating disjoint subsets of deformation-related singular bases into quarters, according to $\Delta \tilde{p}_{\text{mts}} = \{0.5 \cdot (p-1) + \gamma_{\text{offset}}^{(i)} \mid p \in \mathbb{N}, p \leq \tilde{N}_B\}$ mm, where $\{\gamma_{\text{offset}}^{(i)} \mid i=1,2,3,4\} = \{0.0, 12.5, 25.0, 37.5\}$ mm, and $\tilde{N}_B = 25$. The overlapping integral with these reduced bases $\langle \hat{\Psi}_\rho | \tilde{\Psi}_{\rho'}^{(i)} \rangle$, elucidates the shared spatial modal characteristics, providing a deeper understanding of the contributions arising from non-overlapping

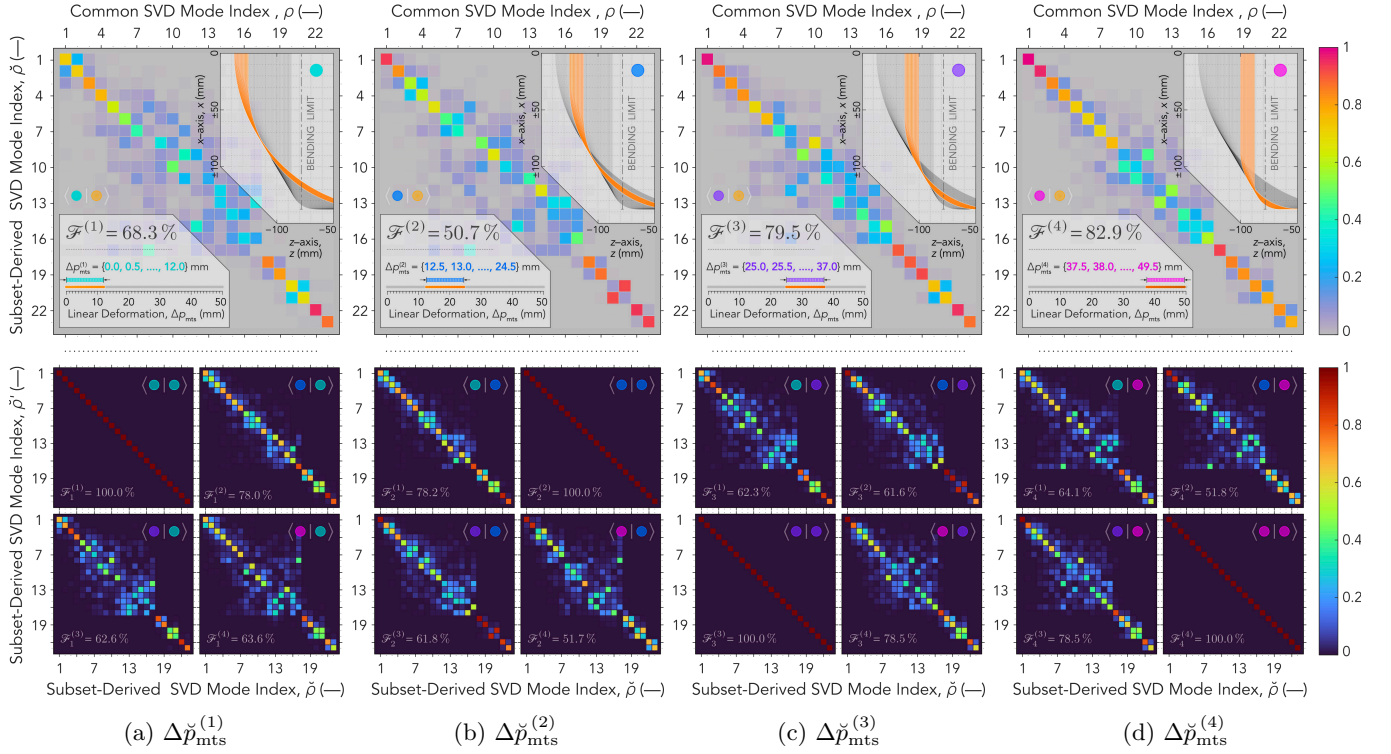


FIG. 9: To consider the similarity of the bend-resolved set for a different range of mechanical movements, the overlap integral analysis examining the contributions of disjoint deformation subsets by comparing the comprehensively spanned bend-resolved singular basis to their subset-derived counterparts, $\langle \hat{\Psi}_\rho | \check{\Psi}_{\rho'}^{(i)} \rangle$ at the top of (a, b, c, d), accompanied by matrices at the bottom of (a, b, c, d) representing the basis transformations between the subset-derived SVD sets themselves, $\langle \check{\Psi}_\rho^{(j)} | \check{\Psi}_{\rho'}^{(i)} \rangle$. Across all scenarios, it is unequivocally evident that intermodal interactions under LG_{00} coupling are predominantly confined to distinct groups of modes, hierarchically ranked according to their associated singular value. Note: $\Delta \check{p}_{\text{mts}}^{(i)} = \{0.5 \cdot (p - 1) + \gamma_{\text{offset}}^{(i)} \mid p \in \mathbb{N}, p \leq \check{N}_B\}$ mm, where $\{\gamma_{\text{offset}}^{(i)} \mid i=1,2,3,4\} = \{0.0, 12.5, 25.0, 37.5\}$ mm, and $\check{N}_B = 25$.

deformation spans, as depicted at top of Fig. 9. These contributions are otherwise seamlessly incorporated into the fully spanned bend-resolved common basis depicted in Fig. 7. As shown at the top of Fig. 9, the last two subset-derived sets of modes, corresponding to deformation ranges $\{\Delta \check{p}_{\text{mts}}^{(i)} \mid i=3,4\} = \{\{25.0, 25.5, \dots, 37.0\}, \{37.5, 38.0, \dots, 49.5\}\}$ mm, emerge from tighter deformation regimes and thus encapsulate more progressive variations in the output field dynamics. These subsets achieve fidelities of $\mathcal{F}^{(3)} = 79.5\%$ and $\mathcal{F}^{(4)} = 82.9\%$, respectively, reflecting their alignment with the global modal framework. Conversely, deformation sets associated with lower curvature, characterized by less progressive field variations (see Figs. 6b and 6c), and defined as $\{\Delta \check{p}_{\text{mts}}^{(i)} \mid i=1,2\} = \{\{0.0, 0.5, \dots, 12.0\}, \{12.5, 13.0, \dots, 24.5\}\}$ mm, exhibit a comparatively weaker correspondence to the fully spanned common basis, with fidelities $\mathcal{F}^{(1)} = 68.3\%$ and $\mathcal{F}^{(2)} = 50.7\%$, highlighting their reduced alignment with the overarching modal basis. The lower fidelity of the second subset of deformations is attributed to an

SVD ambiguity, wherein the modes $\check{\Psi}_\rho^{(2)} \mid_{\rho=\{21,22\}}$ are interchanged. Resolving this ambiguity would result in an alignment with the fully spanned basis of $\approx 70.0\%$, representing a more precise correspondence between the deformation subsets and the overarching modal set. The transformation matrices between the disjoint deformation subsets, shown at the bottom of Fig. 9, naturally exhibit the highest correlation between neighboring sets of deformations. This characteristic remains evident even when the span of deformations is divided into smaller subsets ($N_M > \check{N}_B$). As shown in Fig. 9, the group of lower-order modes, $\check{\Psi}_\rho \mid_{\rho \in \{1, \dots, 7\}}$, consistently displays a predominantly diagonal structure, even when comparing the common basis to disjoint subset-derived bases. This diagonal dominance becomes increasingly pronounced for subsets corresponding to tighter bends. Lower-order modes, characterized by spatial profiles that are more strongly confined to the fiber core, are less susceptible to intermodal coupling and therefore remain a major component of the modal space. In contrast, middle-order modes are less confined to the core, with effective refractive indices (n_{eff}) closer to the

cladding index, rendering them more vulnerable to mode coupling and distortion. These middle-order modes $\check{\Psi}_\rho |_{\rho \in \{8, \dots, 16\}}$, often become ambiguous as multiple modes blend together, exhibiting variability in their coupling patterns due to their heightened sensitivity to changes in bending radius or deformation profiles. Conversely, the highest-order modes $\check{\Psi}_\rho |_{\rho \in \{17, \dots, 23\}}$ is effectively isolated, with minimal power exchange among its members. This isolation arises as the highest-order modes approach their cutoff condition under tighter bends, where the critical angle (θ_c) is exceeded. Beyond this threshold, these modes transition into radiative or leaky states, as the conditions required for guided field propagation are no longer met. Consequently, the modes experience significant attenuation due to energy dissipation into the cladding or radiation into the surrounding medium. This rapid loss severely limits the effective interaction length, reducing the potential for meaningful coupling between radiative modes, even in the presence of spatial overlap. The combination of high loss and diminished interaction length ensures that energy exchange between these highest-order modes becomes negligible.

IV. DISCUSSION

Under realistic experimental conditions, such as those illustrated in Fig. 4a, it is reasonable to assume that fiber bends do not occur strictly within an idealized single plane. Instead, the intrinsic twisting of the fiber, combined with the interaction of unperturbed modes, likely facilitates additional energy exchange through micro-bends, thereby adding complexity to the modal dynamics. The controlled bending of the fiber was achieved by precisely manipulating a linear translation stage (Δp_{mts}) using the V-groove adapter, which formed two consistent bends with progressively decreasing radii, positioned ahead of the permanently clamped straight sections of the fiber. To account for practical considerations, the fiber was pre-bent in its initial state, ensuring that the output field was not exclusively governed by differential modal phase delays between non-degenerate mode groups propagating through the fiber. It has been observed that the emergent speckle patterns exhibit significantly reduced variation when the optical field is coupled near the core-cladding interface, suggesting that a substantial portion of the power predominantly coupled into higher-order modes fails to recouple into the fundamental modes and instead dissipates into the cladding. This behavior aligns with findings in imaging applications, where fiber deformation induces image scrambling within the core while only gradual intensity attenuation occurs at the periphery^{28,43,44}. The complexity of dynamic transformations in the evolved field, driven by lateral shifts of the input fields, is modulated by the presence of orbital angular momentum. While the dynamic variations in the speckle basis provide valuable insights into field similarity arising

from intermodal coupling, they significantly overestimate the fiber's modal bandwidth. By employing dimensionality reduction techniques, the captured fiber conformations can be condensed into bases that effectively span the fiber's modal space. A subsequent dimensionality reduction on these bases reveals a robust, deformation-adaptive basis that encapsulates the differential changes induced by fiber deformation⁴⁵. Although different coupling scenarios with LG modes result in varying spatial distributions of singular modes associated with fiber deformation, the application of a second SVD produced a common basis set with nearly indistinguishable spatial characteristics. This set preserves its spatial integrity, even when different subsets of speckle patterns or singular sets from the linear displacement of the translation stage are incorporated into the second SVD. The modes differ only in phase due to the inherent sign ambiguity of the SVD, which is also unique up to the permutation of singular vectors with an equal coupling strengths. In this basis, the modes with the lowest and highest coupling strengths exhibit not only a high degree of spatial symmetry, consistent with the entire set, but also a striking resemblance to degenerate fiber modes. We assume that this robust basis provides an optimal linear superposition of fiber modes, facilitating the most dominant differential power exchange between distorted singular modes while effectively incorporating all fiber conformations within a given U-shaped configuration⁴⁶. The overall change in the fiber's modal basis is predominantly determined by the varying span of deformations and can be appropriately projected onto bend-resolved modes, regardless of whether orbital angular momentum (OAM) is involved in coupling into the fiber. As the low- and mid-order singular mode sets exhibit differential sensitivity to external perturbations, higher-sensitivity modes can be harnessed for real-time detection of mechanical impairments. Concurrently, advanced transmission strategies can selectively exploit modes with consistent differential mode GD or confine excitation to lower-order modes, optimizing the deployment of FMFs by balancing the high-capacity transmission of MMFs with the intrinsic stability of SMFs, all while preserving signal integrity⁴⁷.

V. CONCLUSION

Our bend-defined modes provide a method for defining a specific mode set directly linked to mechanical variations in the fiber. When bending conditions change, a significant alteration in modal orthogonality is observed. We anticipate that this approach can be employed to monitor structural changes in both stationary and dynamically moving optical fibers, facilitating the identification of mechanical shifts in fiber deployment. Further investigation into selective mode launching and the separation of orthogonal modes could establish a direct correlation between spatial mode structure and fiber deformation, enabling an approximation of bending profiles

in a given fiber. While mode degeneracies and the non-uniqueness of modal evolution may limit exact reconstructions, analyzing these mode transitions could still provide valuable insights into fiber deformations. Our approach can be readily integrated into fiber-based imaging and communication systems to assist in recovering scrambled phase and intensity information from few-mode and multi-mode fibers. In fiber imaging applications, this analytical framework has the potential to enhance image quality in dynamic fiber systems by tracking and compensating for changes in the fiber's modal basis, despite the challenges posed by mode degeneracies and the inherent ambiguities of modal evolution. However, achieving real-time correction may require advanced computational techniques to mitigate rapid and unpredictable modal fluctuations. In fiber communications, particularly those incorporating coherent MIMO DSP, this analytical approach could serve as a tool for detecting eavesdropping attempts or identifying structural modifications in installed infrastructure. By monitoring deviations in bend-resolved modes, the system could detect motion in the fiber exceeding its calibrated range, indicating potential external disturbances or mechanical shifts.

ACKNOWLEDGMENTS

The work was supported by the Horizon 2020 Future and Emerging Technologies Open grant agreement "Super-pixels" No. 829116 and the EPSRC (grant No. EPSRC EP/T009047/1).

DATA AVAILABILITY STATEMENT

The data supporting the findings of this study are available from the corresponding author upon reasonable request.

- ¹P. Lu, N. Lalam, M. Badar, B. Liu, B. T. Chorpene, M. P. Buric, and P. R. Ohodnicki, *Applied Physics Reviews* **6**, 041302 (2019).
- ²K. C. Galloway, Y. Chen, E. Templeton, B. Rife, I. S. Godage, and E. J. Barth, *Soft Robotics* **6**, 671 (2019).
- ³S. Hussain, A. Ghaffar, S. H. Abbas Musavi, M. Mehdi, M. Ahemd, Y. Jianping, C. Lei, R. Mehdi, and I. Mehdi, *Optical Fiber Technology* **81**, 103559 (2023).
- ⁴I. Lior, D. Rivet, J.-P. Ampuero, A. Sladen, S. Barrientos, R. Sánchez-Olavarría, G. A. Villarroel Opazo, and J. A. Bustamante Prado, *Scientific Reports* **13**, 424 (2023), publisher: Nature Publishing Group.
- ⁵Z. Zhang, G. Yin, R. Jiang, S. Gu, H. Lu, K. Liu, D. Li, and T. Zhu, *Journal of Lightwave Technology* **41**, 6838 (2023).
- ⁶R.-J. Essiambre and R. W. Tkach, *Proceedings of the IEEE* **100**, 1035 (2012).
- ⁷R. W. Tkach, *Bell Labs Technical Journal* **14**, 3 (2010).
- ⁸M. Nakazawa, M. Suzuki, Y. Awaji, and T. Morioka, eds., *Space-Division Multiplexing in Optical Communication Systems: Extremely Advanced Optical Transmission with 3M Technologies*, Springer Series in Optical Sciences, Vol. 236 (Springer International Publishing, Cham, 2022).
- ⁹P. J. Winzer and D. T. Neilson, *Journal of Lightwave Technology* **35**, 1099 (2017), conference Name: Journal of Lightwave Technology.
- ¹⁰A. A. Juárez, C. A. Bunge, S. Warm, and K. Petermann, *Optics Express* **20**, 13810 (2012), publisher: Optica Publishing Group.
- ¹¹W. Klaus, P. J. Winzer, and K. Nakajima, *Proceedings of the IEEE* **110**, 1619 (2022), conference Name: Proceedings of the IEEE.
- ¹²P. Sillard, M. Bigot-Astruc, and D. Molin, *Journal of Lightwave Technology* **32**, 2824 (2014), conference Name: Journal of Lightwave Technology.
- ¹³M. v. d. Hout, G. D. Sciuillo, R. S. Luís, B. J. Puttnam, N. K. Fontaine, R. Ryf, H. Chen, M. Mazur, D. T. Neilson, P. Sillard, F. Achten, A. Mefleh, J. Sakaguchi, C. Antonelli, C. Okonkwo, H. Furukawa, and G. Rademacher, *Journal of Lightwave Technology* **42**, 1136 (2024), publisher: IEEE.
- ¹⁴Y. Zhou, B. Braverman, A. Fyffe, R. Zhang, J. Zhao, A. E. Willner, Z. Shi, and R. W. Boyd, *Nature Communications* **12**, 1866 (2021), publisher: Nature Publishing Group.
- ¹⁵P. J. Winzer, D. T. Neilson, and A. R. Chraplyvy, *Optics Express* **26**, 24190 (2018), publisher: Optica Publishing Group.
- ¹⁶Y. Liu, G. Li, Q. Qin, Z. Tan, M. Wang, and F. Yan, *Optics & Laser Technology* **131**, 106424 (2020).
- ¹⁷X. Wang, Y. Wang, K. Zhang, K. Althoefel, and L. Su, *Scientific Reports* **12**, 12684 (2022), publisher: Nature Publishing Group.
- ¹⁸D. Bender, U. Çakır, and E. Yüce, *IEEE Sensors Journal* **23**, 6956 (2023), conference Name: IEEE Sensors Journal.
- ¹⁹Y. Zheng, R. J. Kilpatrick, D. B. Phillips, and G. S. D. Gordon, "Self-attention-based non-linear basis transformations for compact latent space modelling of dynamic optical fibre transmission matrices," (2024), arXiv:2406.07775 [cs].
- ²⁰S. SeyedinNavadeh, M. Milanizadeh, F. Zanetto, G. Ferrari, M. Sampietro, M. Sorel, D. A. B. Miller, A. Melloni, and F. Morichetti, *Nature Photonics* **18**, 149 (2024), publisher: Nature Publishing Group.
- ²¹D. A. B. Miller, *Journal of Lightwave Technology* **31**, 3987 (2013), conference Name: Journal of Lightwave Technology.
- ²²R. Yadav, F. A. Barbosa, and F. M. Ferreira, *Journal of Lightwave Technology* **42**, 3695 (2024), conference Name: Journal of Lightwave Technology.
- ²³F. Kettlun, F. Rosas, and C. Oberli, *EURASIP Journal on Wireless Communications and Networking* **2021**, 151 (2021).
- ²⁴D. Stellinga, D. B. Phillips, S. P. Mekhail, A. Selyem, S. Turtaev, T. Čizmár, and M. J. Padgett, *Science* **374**, 1395 (2021), publisher: American Association for the Advancement of Science.
- ²⁵M. Stibůrek, P. Ondráčková, T. Tučková, S. Turtaev, M. Šiler, T. Pikálek, P. Jákl, A. Gomes, J. Krejčí, P. Kolbábková, H. Uhlířová, and T. Čizmár, *Nature Communications* **14**, 1897 (2023).
- ²⁶P. Jákl, M. Šiler, J. Ježek, A. Cifuentes, J. Trägårdh, P. Zemánek, and T. Čizmár, *Photonics* **9**, 37 (2022).
- ²⁷S. Resisi, Y. Viernik, S. M. Popoff, and Y. Bromberg, *APL Photonics* **5**, 036103 (2020).
- ²⁸S. Li, S. A. R. Horsley, T. Tyc, T. Čizmár, and D. B. Phillips, *Nature Communications* **12** (2021), 10.1038/s41467-021-23729-1.
- ²⁹M. W. Matthès, Y. Bromberg, J. de Rosny, and S. M. Popoff, *Physical Review X* **11**, 021060 (2021), publisher: American Physical Society.
- ³⁰H. Cao, T. Čizmár, S. Turtaev, T. Tyc, and S. Rotter, *Advances in Optics and Photonics* **15**, 524 (2023).
- ³¹S. Rothe, N. Koukourakis, H. Radner, A. Lonnstrom, E. Jorswieck, and J. W. Czarnecki, *Scientific Reports* **10**, 2740 (2020), publisher: Nature Publishing Group.
- ³²L. V. Amitonova, T. B. H. Tentrup, I. M. Vellekoop, and P. W. H. Pinkse, *Optics Express* **28**, 5965 (2020), publisher: Optica Publishing Group.
- ³³C. K. Mididoddi, R. J. Kilpatrick, C. Sharp, P. del Hougne, S. A. R. Horsley, and D. B. Phillips, *Nature Photonics*, 1 (2025), publisher: Nature Publishing Group.

- ³⁴Z. Zhao, X. Li, S. Yan, K. Tian, X. Wang, H. Zhao, E. Lewis, G. Farrell, and P. Wang, *Optics Letters* **49**, 1329 (2024), publisher: Optica Publishing Group.
- ³⁵M. Elsharif, A. E. Sali, M. G. Muñoz, F. Alam, B. AlQattan, D. S. Antonysamy, M. F. Zaki, A. K. Yetisen, S. Park, T. D. Wilkinson, and H. Butt, *Advanced Photonics Research* **3**, 2100371 (2022).
- ³⁶M. Veetikazhy, A. Kragh Hansen, D. Marti, S. Mark Jensen, A. Lykke Borre, E. Ravn Andresen, K. Dholakia, and P. Es-kil Andersen, *Optics Express* **29**, 11819 (2021).
- ³⁷H. Kupianskyi, S. A. R. Horsley, and D. B. Phillips, *Optica* **11**, 101 (2024), publisher: Optica Publishing Group.
- ³⁸D. A. B. Miller, *Advances in Optics and Photonics* **11**, 679 (2019).
- ³⁹K.-P. Ho and J. M. Kahn, *Journal of Lightwave Technology* **32**, 614 (2014), conference Name: Journal of Lightwave Technology.
- ⁴⁰H. Uhlřřová, M. Stibůřek, T. Pikálek, A. Gomes, S. Turtaev, P. Kolbábřková, and T. Čizřřár, *Neurophotonics* **11**, S11504 (2024), publisher: SPIE.
- ⁴¹I. T. Leite, S. Turtaev, D. E. Boonzajer Flaes, and T. Čizřřár, *APL Photonics* **6**, 036112 (2021).
- ⁴²T. Tučřřková, M. Šiler, D. E. Boonzajer Flaes, P. Jákł, S. Turtaev, S. Kráťřřký, R. Heintzmann, H. Uhlřřová, and T. Čizřřár, *Optics Express* **29**, 38206 (2021).
- ⁴³S. P. Mekhail and M. J. Padgett, in *Quantum Sensing, Imaging, and Precision Metrology II*, Vol. 12912 (SPIE, 2024) pp. 207–209.
- ⁴⁴D. E. Boonzajer Flaes, J. Stopka, S. Turtaev, J. F. De Boer, T. Tyc, and T. Čizřřár, *Physical Review Letters* **120**, 233901 (2018).
- ⁴⁵J. Xu and X. Xiao, “Principal modes of multimode fibers resisting fiber bending,” (2023), arXiv:2311.04004 [physics].
- ⁴⁶M. Lan, Y. Xiang, J. Li, L. Gao, Y. Liu, Z. Wang, S. Yu, G. Wu, and J. Ma, *Optics Express* **28**, 13662 (2020), publisher: Optica Publishing Group.
- ⁴⁷P. Sillard, K. Benyahya, D. Soma, G. Labroille, P. Jian, K. Igarashi, R. Ryf, N. K. Fontaine, G. Rademacher, and K. Shibahara, *Proceedings of the IEEE* **110**, 1804 (2022).
- ⁴⁸M. Plöschner, T. Tyc, and T. Čizřřár, *Nature Photonics* **9**, 529 (2015).

Appendix A: Volumetric visualization

The volumetric visualization of the selected set of experimentally acquired speckle patterns in Fig. 1a, which were generated under constant injection with a fixed displacement at the proximal facet, i.e. $E_\mu^{(p)}(r, \theta | z = 0) \equiv E_\mu(r, \theta)$, systematically illustrates their evolution as the fiber’s deformation is progressively altered by MTS. As the injected light at the same position on the fiber facet, using different $\{LG_{\ell 0} | \ell \in \{\pm 1, 0\}\}$, excites the fiber modes with varying efficiencies, the resulting output fields must also differ. Nevertheless, as shown in the cross-section of their quarter-volume (see Fig. 1a), significant similarities persist, with the addition of orbital angular momentum specifically enhancing the fraction of total power coupled into higher-order modes, which would otherwise couple into the fundamental modes with a Gaussian spot. However, since all speckle patterns differ due to varying power distribution across the modal space under different coupling conditions, the total cumulative power for all speckles and deformations exhibits a high correlation across different LG couplings (see Fig. 1b), as well as the cumulative sum of speckles per deformation, depicted in the

slices $(x_0, y_0) = \{(\pm r, 0), (0, \pm r)\}$. Moreover, it is clearly evident that the power tends to accumulate in all three cases along the $-x$ direction, with a predominant symmetry around the y -axis. Compared to simulations with a non-deformed straight fiber, this behavior only occurs when all input fields, equidistantly separated on a square Cartesian grid, have an additional phase tilt. Specifically, when the input field at the central position $(\nu, \nu) = (0, 0)$ has zero or negligible additional phase tilt relative to the diameter of the fiber core (i.e., the wavefront from the SLM’s 1st diffraction order in the experiments is nearly parallel to the proximal fiber facet), the cumulative output power exhibits a spatially balanced, flat-top profile at the distal fiber facet. Only when the wavefronts of all displaced fields coupled into the fiber are predominantly tilted in an arbitrary plane does the output power tend to accumulate in the same direction as the global tilt of the input fields. Nevertheless, since the global tilt of the input wavefronts has been minimized within the experimental configuration, the spatially balanced accumulation of power around the y -axis at the distal facet, directed along the $-x$ axis, can be distinctly attributed to the U-shaped fiber bend configuration. As mentioned previously, the fiber undergoes an initial bend from the $-x$ to the $+x$ direction within the xz -plane, while maintaining a constant position in the xy -plane (see Fig. 4).

Appendix B: Correlative Analysis

To offer a detailed insight into the dynamic distribution of the optical field associated with fiber deformation, the correlation matrices of the overlap integrals are presented in Fig. 10. These correlation matrices represent the inner products of a set of normalized speckles that evolve during the deformation for a fixed displacement of the injected beam, expressed as $[\langle \widehat{S}_\mu^{(p)} | \widehat{S}_\mu^{(q)} \rangle] = \mathbf{C}_\mu$, where $\widehat{S} = S \|S\|^{-1}$ and $\mathbf{C}_\mu \in \mathbb{C}^{N_B \times N_B}$. The middle volumetric plot illustrates the dynamic changes in correlation matrices for input modes along the diagonal plot of cumulative power across bends $\{(\nu, \nu) | \nu = \nu\}$, as shown at the top in Fig. 10. The highlighted cross-section in the volumetric visualization indicates the position of the correlation matrix for $\mu(0, 0)$, which is separately depicted at the bottom. It is apparent that, while the cumulative power through all deformations with LG_{00} is nearly uniformly redistributed across the fiber facet, its counterparts with $LG_{\pm 10}$ exhibit a more pronounced, unbalanced power profile that appears to be mutually opposite. Comparing the correlation matrices (see the sides in the volumetric plot in Fig. 10), a higher structural similarity is observed between coupling with LG_{00} and LG_{-10} for input modes $\{(\nu, \nu) | \nu = \nu < 0\}$, while LG_{00} and LG_{+10} exhibit a higher similarity for $\{(\nu, \nu) | \nu = \nu > 0\}$. These matrices show that optical mode power remains invariant as they evolve under controlled bending, offering insights into the fiber’s structural and modal stability.

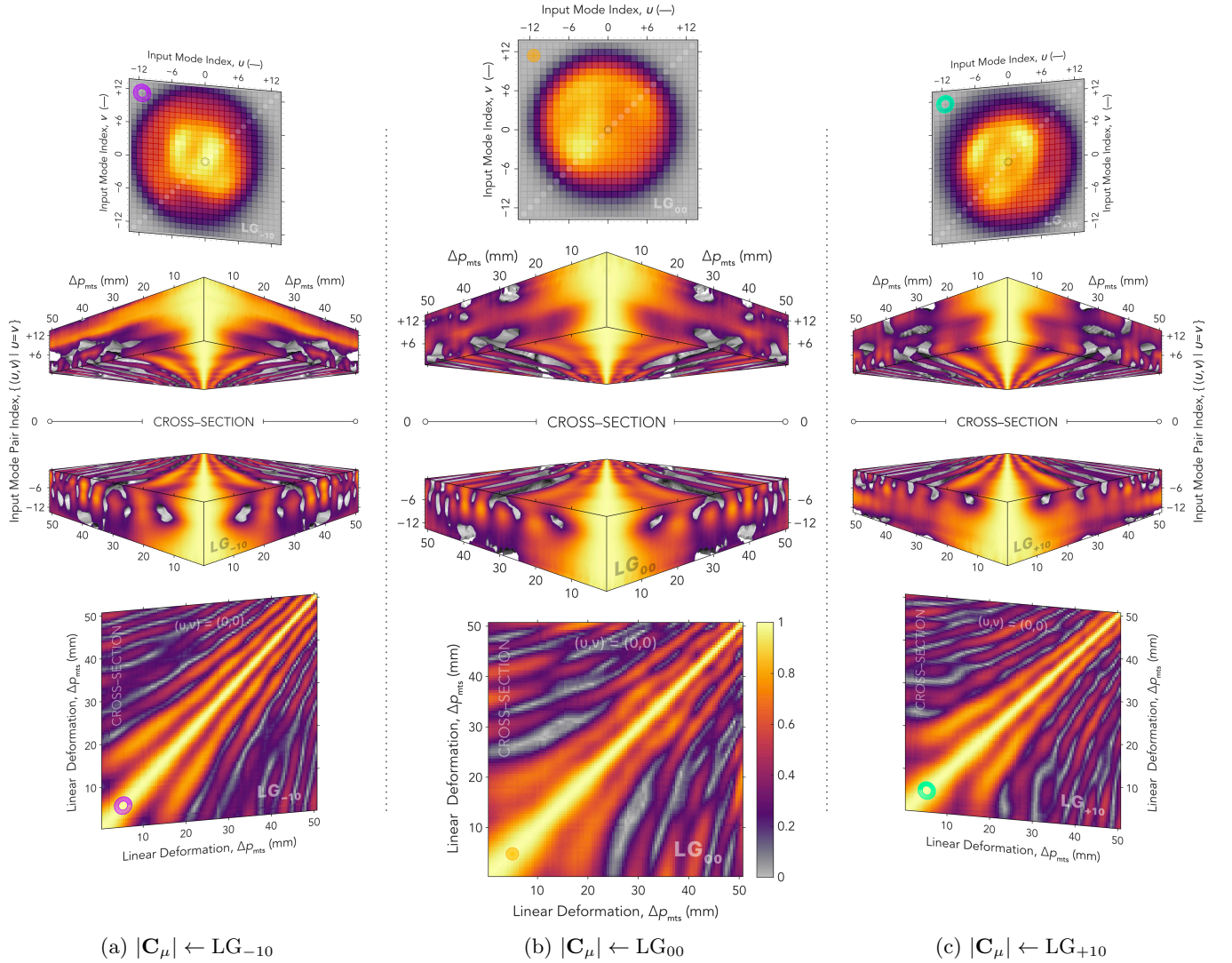


FIG. 10: Correlative analysis of speckle pattern emerged in response to linear deformation under constant displacement of the injected beam. Above: Total power through all linear deformations as a function of displacement of input field, $\bar{P}(v, \nu) = \text{vec}_{v\nu}^{-1} \{ (N_B N_{px})^{-1} \sum_{p=1}^{N_B} \sum_{i=1}^{N_{px}} |S_\mu^{(p)}(x_i, y_i)|^2 \}$. Middle: Stacked visualization of correlation matrices constructed from emerging speckle patterns under varying deformation as $[\langle \hat{S}_\mu^{(p)} | \hat{S}_\mu^{(q)} \rangle] = \mathbf{C}_\mu$, while maintaining the position of the injected beam at the entrance of the fiber for pairs of input modes $\{(v, \nu) \mid v = \nu \neq 0\}$. Bellow: Correlation matrix at the cross-section of the matrix stack for input mode pair $(v, \nu) = (0, 0)$. Notes: $|C_\mu| \in [0, 1]$, where lower limit indicates completely uncorrelated fields and upper limit perfect correlation in amplitude and phase.

Appendix C: Alignment with Theoretical Eigensolutions

The theoretical number of guided LP modes, determined to be $N_M = 23$ for light injection at $\lambda = 852$ nm, based on the fiber's parameters within specified tolerances provided by the manufacturer, SiO₂ core with $\varnothing_{\text{core}} = (25 \pm 3) \mu\text{m}$, F:SiO₂ cladding with $\varnothing_{\text{cladd}} = (125 \pm 2) \mu\text{m}$, NA = 0.100 ± 0.015 . Using the mean values provided by the manufacturer, this result was calculated via an analytically solved eigenvalue equation under the weak guidance approximation and found to be consistent with experimentally obtained SVD modes, see Fig. 11.

Appendix D: Experimental Implementation

A simplified schematic diagram of the experimental optical arrangement is shown in Fig. 4a. A volume-holographic-grating (VHG) wavelength-stabilized laser diode with a narrow linewidth operating at $\lambda = (852 \pm 1) \text{ nm}$ was used as the light source. The beam was collimated by a fixed-focal-point air-spaced doublet after passing through a 1 m long SM polarization-maintaining fiber (PMF) terminated on both ends with FC/APC connectors. The subsequent half-wave plate (HWP) rotates the linearly polarized beam to be parallel with the ex-

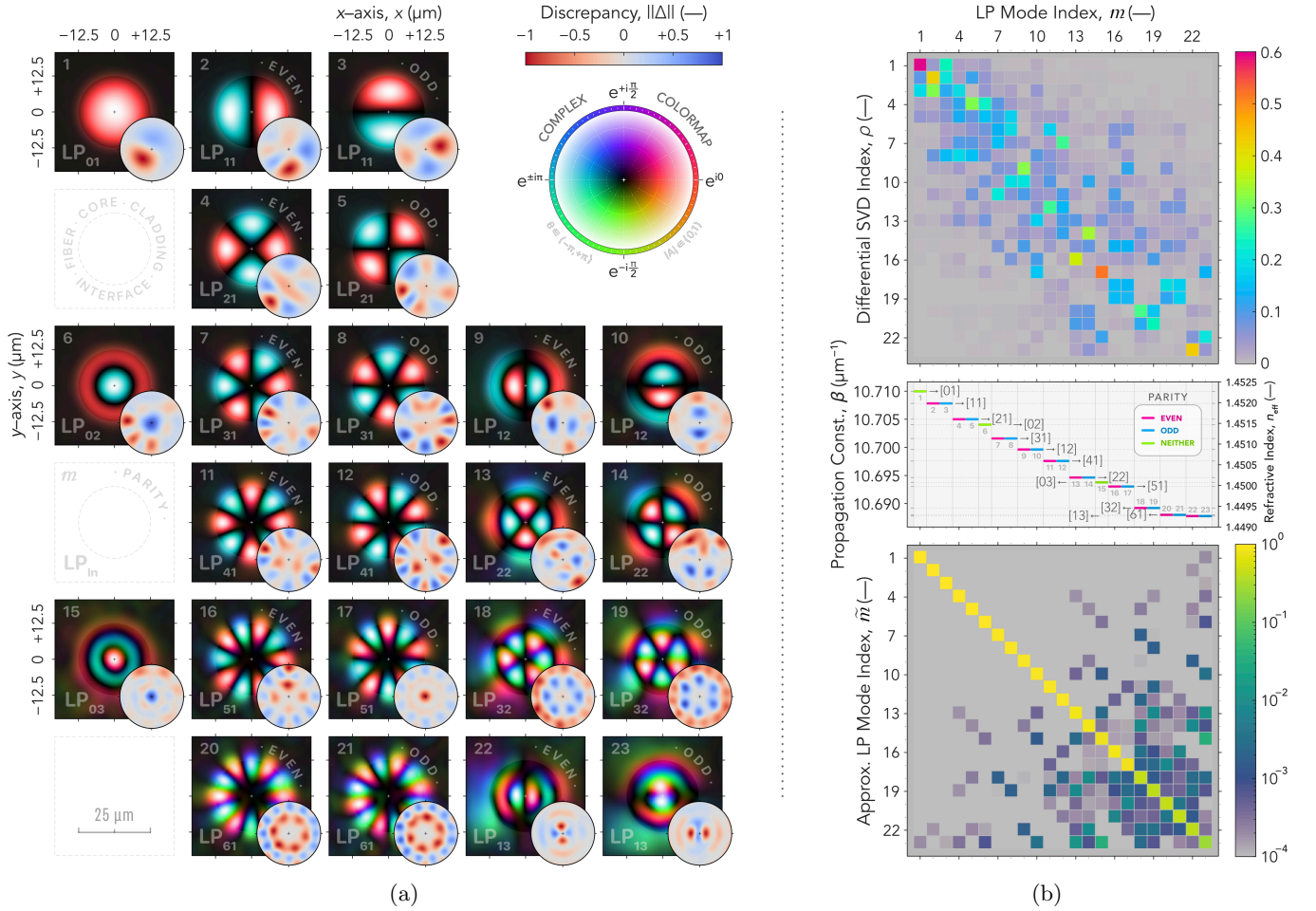


FIG. 11: Projection of the bend-resolved singular basis ($\hat{\Psi}_\rho$) inferred from experimental measurements onto the weakly guiding approximative LP modes. (a) Spatial profiles of the approximated modes, accompanied by the normalized discrepancy from the ideal theoretical profiles, exhibiting discrepancies reduced by several orders of magnitude. Includes the complex colormap used throughout the manuscript, which maps complex numbers into a colored phase with a linear amplitude transition between black and white. (b) Top: Transformation matrix representing the correspondence between the theoretical LP modes and the experimentally determined bend-resolved common singular basis. Middle: Visualization of the modal propagation constants (β_m) alongside their corresponding effective refractive indices (n_m^{eff}). Bottom: Error matrix quantifying the discrepancies between the reconstructed LP basis and the ideal theoretical LP modes, displayed on a logarithmic scale and demonstrating pronounced diagonal dominance. Note: $N_M = 23$ at $\lambda = 852$ nm, modal angular (l) and radial (n) number mapped to $m = m(l, n)$, where $m \in \mathbb{N}$.

traordinary axis of the nematic liquid crystals on silicon (LCoS) of the SLM, achieving a solely voltage-dependent phase shift with a maximum diffraction efficiency. A pair of achromatic positive doublet lenses (L1, L2) are used to expand the beam to sufficiently overfill the available (15.36 × 9.60) mm active area of the SLM chip with near-uniform illumination. After filtering the 0th diffraction order in the Fourier domain with an aperture between the lenses L3 and L4, the collimated beam of targeted 1st diffraction order was demagnified with another lens pair (L5, L6) to closely match the acceptance angle of the fiber core. The generated holograms positioned at the centre of the SLM's Fourier plane, with a resolution of (1900 × 1200) px and a pixel pitch of (8 × 8) μm, are

projected onto the proximal (near) facet of the fiber via an achromatic microscope objective. This objective has a magnification of 20×, where the mode field diameter (MFD) of the fiber was digitally controlled via holograph spatial amplitude modulation to precisely adjust the diameter of the light beam coupled into the fiber. Complex spatial modulation allowed for fiber coupling of arbitrary base function, such as Laguerre–Gaussian (LG_{±*l**p*}) or Hermite–Gaussian (HG_{*nm*}). The fiber has a total length of $L_T = (1.000^{+0.075}_{-0.000})$ m including the FC/PC connectors. Overfilling the numerical aperture (NA) can lead some incident light being coupled into cladding (i.e. radiation) modes that can sufficiently propagate even over longer distances of fiber, leading to increased background

in the output wavefront emitted at the distal (far) end of the fiber. The fiber is deliberately arranged in a U-shaped configuration with permanently clamped center point to achieve predictable planar bends exclusively on its semicircular arc sections either side of this fixed point (i.e., the y -axis of the fiber remains in the xz -plane), as detailed further in E. A motorised translation stage (MTS) with a linear travel range $\Delta p_{\text{mts}} = (0-50)$ mm has been used for controlled and highly repeatable bidirectional deformation (compression–expansion) of the fiber with an accuracy of $\varepsilon_{\text{mts}} = \pm 1.6 \mu\text{m}$. Subsequently, the speckled near-fields arising at the distal facet, with imprinted fiber conformations resulting from the step-wise movement of the MTS, are projected onto a camera (CAM) through a short focal length aspheric lens (L7) combined with a long focal length achromatic doublet (L8). Before that, the object beam is combined with an external reference beam on a non-polarizing beamsplitter (BS2) at a mutually non-zero axial angle to enable fast holographic complex field acquisition from single-frame interferograms. The reference beam, taken from a non-polarizing beamsplitter (BS1), is deliberately delayed by a pair of mirrors to minimize the optical-path difference (OPD), considering the phase delay introduced by the fiber length. It is then expanded via a pair of lenses (L9, L10) to achieve a near-uniform planar wavefront for off-axis digital holography. Absorptive filters (ND1, ND2) are used accordingly to achieve high-dynamic mutual modulation while avoiding overexposure in the region of interest (ROI) within the camera’s full-frame resolution of (5328×3040) px. The incoherent light source (LED) with $\lambda_0 = 850$ nm and bandwidth $\Delta\lambda = 55$ nm is used to minimize defocus in the projected wide-field image of the fiber’s distal facet on the CAM. As an extended source, it is only roughly collimated with an aspheric condenser lens (L11) and a long focal length achromatic doublet (L12). The projection of the proximal facet onto the CAM is achieved in the same manner, even though it is not shown in the schematic for simplicity. Note that all lenses have been experimentally aligned appropriate image replay, despite inconsistent focal lengths in Fig. 4a.

Appendix E: Geometry of the Fiber Bending Path

As previously outlined, ensuring predictable deformation of the fiber during experiments, as demonstrated in Fig. 4a, is pivotal for achieving precise and reproducible approximation of measurements. The fiber is permanently mounted in two parallel V-groove holders, equally separated by distance $D = 2R_0$ in xz -plane, to achieve an ideal semicircular arc section of constant curvature $\rho(R_0) \propto R_0^{-1}$, defined by a nominal radius $R_0 = 137.5$ mm. This constrains the fiber to a specific geometric shape that can be longitudinally deformed on the flexible semicircular segment in a deterministic manner between the inner edges of both holders acting as static nodes, eliminating the need for any additional movement

of optical parts during its deformation (see Fig. 4b). The bidirectional deformation is conducted using a linear MTS displacement (Δp_{mts}) with a one-sided V-groove restrainer holding the fiber at its midpoint during the compression–expansion process. This U-shaped configuration preferentially creates additional straight segments connected via two quarter-circle arcs with a constant curvature, as illustrated in Fig. 4b. The entire dynamic process can be encoded through a constant number of segments ($N_{\text{seg}} = 7$) with precisely defined curvatures and lengths, where segments $s \in \{3, 5\}$ are bent, while segments $s \in \{1, 2, 4, 6, 7\}$ remain straight. Considering the initial semicircular geometry, the radius of the bent segments (r_{B}) decreases linearly with the linear deformation applied by MTS displacement as follows

$$r_{\text{B}}(\Delta p_{\text{mts}}) = R_0 - \Delta p_{\text{mts}} \left(2 - \frac{\pi}{2}\right)^{-1}, \quad (\text{E1})$$

until it gradually reaches the minimum $r_{\text{B}}^{\text{min}} = 21.0$ mm, that is determined by the travel range limit of the MTS. Accordingly to radius decay given by Eq. (E1), the dynamic variation in the length of each segment (L_s) triggered by Δp_{mts} can be mathematically expressed as

$$L_s^{(p)}(r_{\text{B}}) = \begin{cases} \frac{1}{2}(L_{\text{T}} - \pi R_0) & \text{if } s \in \{1, 7\}, \\ \left(R_0 - r_{\text{B}}^{(p)}\right) \left(\frac{\pi}{2} - 1\right) & \text{if } s \in \{2, 6\}, \\ \frac{1}{2}\pi r_{\text{B}}^{(p)} & \text{if } s \in \{3, 5\}, \\ 2 \left(R_0 - r_{\text{B}}^{(p)}\right) & \text{if } s = 4, \end{cases} \quad (\text{E2})$$

while the cumulative sum of all segmental lengths must preserve the total length of the fiber for any arbitrary deformation of Δp_{mts} , strictly following the expression

$$L_{\text{T}} = \sum_{s=1}^{N_{\text{seg}}} L_s^{(p)} \quad \forall p \in \{1, \dots, N_{\text{B}}\}. \quad (\text{E3})$$

The bending limit in Fig. 4b can be achieved if the bent segments radius, centred and linearly shifting over the hypotenuse with a defined length of $R_0\sqrt{1 + (2 - \pi/2)^2}$, theoretically reaches $r_{\text{B}}(R_0(2 - \pi/2)) = 0$. This implies that the curved segments disappear as $\rho(r_{\text{B}}) \rightarrow \infty$, theoretically bending the neutral axis of the fiber at a right angle (discontinuous bend), resulting in the middle and side straight segment lengths of $L_4 = 2R_0$ and $L_{\{2,6\}} = R_0(\pi/2 - 1)$. The semi-transparent area in Fig. 4b approximates the span covered in the xz -plane by the movement of the linear MTS, with curvatures in the range $\rho \approx (7.27 - 47.61) \text{m}^{-1}$, implying that the curvatures are much larger in magnitude than the core radius ($\rho \gg r_{\text{core}}$, where $r_{\text{core}} = 12.5 \mu\text{m}$). The experiments were conducted at discrete positions $\Delta p_{\text{mts}} = \{0.5 \cdot (p - 1) \mid p \in \mathbb{N}, p \leq N_{\text{B}}\}$ mm, corresponding to the positions of the V-groove fiber restrainer in the given coordinate system $z = \{\Delta p_{\text{mts}} - R_0\}$ mm.

The number of bends $N_B = 101$ ensures a thorough evaluation of the bending effects over the specified range, adequately capturing the propagation dynamics of the modes. This comprehensive linear stage translation enables precise tracking of the influence of each deformation position on the overall behavior of modal interactions within a fiber.

Appendix F: Transmission Through Fiber

Building on the previously established geometry based on segmenting the fiber into discrete sections with predictable lengths and curvatures, the dynamic alterations of an optical fiber bending path in a U-shape configura-

tion can be rigorously analyzed. By leveraging deterministic changes in lengths (L_s) and curvatures (ρ_s) into each segment modeled by its own TM, the resulting transmission matrix as a function of altering Δp_{mts} for the entire system can be dynamically described as their product

$$\mathbf{T}(\Delta p_{\text{mts}}) = \prod_{s=N_{\text{seg}}}^1 \mathbf{T}_s^{(p)}(L_s, \rho_s), \quad \text{where } s \in \mathbb{N}. \quad (\text{F1})$$

Considering that the fiber supports a finite number of modes (N_M) at a certain wavelength, where each mode propagates over a given length by its own specific modal propagation constant (β_m), the TMs for straight and bend segments for each deformation of Δp_{mts} with a dimension of $\mathbf{T}_s^{(p)} \in \mathbb{C}^{N_M \times N_M}$ can be, in idealized case, mathematically represented as

$$\underbrace{\mathbf{T}_s^{(p)}(L_s, \rho_s = \infty)}_{\text{straight}} = \begin{bmatrix} e^{i\beta_1 L_s^{(p)}} & 0 & \cdots & 0 \\ 0 & e^{i\beta_2 L_s^{(p)}} & \cdots & 0 \\ \vdots & \vdots & \ddots & \vdots \\ 0 & 0 & \cdots & e^{i\beta_{N_M} L_s^{(p)}} \end{bmatrix} = e^{i\mathbf{B}L_s^{(p)}}, \quad (\text{F2})$$

$$\underbrace{\mathbf{T}_s^{(p)}(L_s, \rho_s \neq \infty)}_{\text{bend}} = \begin{bmatrix} \tau_{11} & \tau_{12} & \cdots & \tau_{1N_M} \\ \tau_{21} & \tau_{22} & \cdots & \tau_{2N_M} \\ \vdots & \vdots & \ddots & \vdots \\ \tau_{N_M 1} & \tau_{N_M 2} & \cdots & \tau_{N_M N_M} \end{bmatrix} = e^{i\tilde{\mathbf{B}}L_s^{(p)}} \approx \sum_{m=1}^{N_M} \frac{1}{(m-1)!} \left[i\tilde{\mathbf{B}}L_s^{(p)} \right]^{m-1}, \quad (\text{F3})$$

where $\mathbf{B} = \text{diag}(\beta_1, \beta_2, \dots, \beta_{N_M})$ is a purely diagonal matrix of modal propagation constants, leading to each mode being multiplied by a single phase factor. In contrast, $\tilde{\mathbf{B}}$ represents a matrix with modified phase factors and off-diagonal terms describing coupling between modes, requiring the modal coefficients to be multiplied by the matrix exponential. Since the matrix $\tilde{\mathbf{B}}$ is diagonalizable, its eigenvalues correspond to the effective propagation constants, while its eigenvectors represent the change in the modal basis in the perturbed fiber. In the first-order approximation, the elements of $\tilde{\mathbf{B}}$ can be expressed as $\tilde{B}_{mm'} = B_{mm'} + K_{mm'}$, where $B_{mm'} = \beta_m \delta_{mm'}$, representing the diagonal terms corresponding to the propagation constants of the uncoupled modes. The coupling matrix, which captures the interaction between different modes due to bending, is defined as $K_{mm'} = \kappa_{mm'}(1 - \delta_{mm'})$, where the off-diagonal coupling coefficients that interact nonlinearly in the exponential function are given by

$\kappa_{mm'} = -n_{\text{core}} k_0 \xi_c \rho^{-1} \langle \Xi_m | x | \Xi_{m'} \rangle$ for $m \neq m'$. These off-diagonal coupling terms are inversely proportional to the curvature of the fiber and depend on the overlap integral between the m -th and m' -th mode, weighted by the position coordinate x along the bend direction⁴⁸. Additionally, the correction factor ξ_c incorporates the photoelastic deformation tensor, accounting for lateral strains relative to longitudinal changes in fused silica, as determined by the Poisson ratio. Subsequently, the dependence of the total TM, as given by Eq. (F1), on the fiber's segmental changes in length and curvature as a function of the applied displacement by Δp_{mts} can be fully expressed by Eqs. (F2) and (F3). In the initial state of the fiber, with the largest radius of curvature, the TM is expressed as a product of four contributing segments $\mathbf{T}(\Delta p_{\text{mts}} = 0) = \mathbf{T}_7 \mathbf{T}_5 \mathbf{T}_3 \mathbf{T}_1$, while the remaining segments $\mathbf{T}_{\{6,4,2\}} \equiv \mathbf{I}$, signify no contribution to the overall transmission.